Computers and Chemical Engineering 142 (2020) 107066

Contents lists available at ScienceDirect

Computers and Chemical Engineering

journal homepage: www.elsevier.com/locate/compchemeng

Multiscale computational fluid dynamics modeling and reactor design of plasma-enhanced atomic layer deposition

Yichi Zhang[a], Yangyao Ding[a], Panagiotis D. Christofides[a,b,*]

[a] Department of Chemical and Biomolecular Engineering, University of California, Los Angeles, CA, 90095-1592, USA
[b] Department of Electrical and Computer Engineering, University of California, Los Angeles, CA 90095-1592, USA

ARTICLE INFO

Article history:
Received 14 July 2020
Revised 17 August 2020
Accepted 17 August 2020
Available online 19 August 2020

Keywords:
Plasma-enhanced atomic layer deposition
Microscopic modeling
Kinetic Monte Carlo modeling
Density functional theory
Computational fluid dynamics
Cycle time optimization

ABSTRACT

Plasma-enhanced atomic layer deposition (PEALD) is one of the most widely adopted deposition methods in the semiconductor industry. It is chosen largely due to its superior ability to deliver ultra-conformal dielectric thin-films with high aspect-ratio surface structures, which are encountered more and more often in the novel design of metal-oxide-semiconductor field-effect transistors (MOSFETs) in the NAND (Not-And)-type flash memory devices. Compared with the traditional thermal ALD method, PEALD allows for lower operating temperature and speeds up the deposition process with the involvement of plasma species. Despite its popularity, the development of PEALD operation policies remains a complicated and expensive task, which motivates the construction of an accurate and comprehensive simulation model. While existing models have described the individual or partially coupled domains, none of these models has captured all three domains in the PEALD process: surface reaction, macroscopic gas transport, and plasma generation. In this work, a comprehensive multiscale computational fluid dynamics (CFD) model is developed for a remote PEALD reactor used in the deposition of HfO_2 thin-films. First, a previously developed kinetic Monte-Carlo (kMC) model is adapted for the multiscale simulation to describe the surface reactions. Then, two macroscopic models, specifically tailored for the remote plasma reactor, are formulated to describe the dynamic behaviors of the plasma generation and bulk species transport domains, respectively. Additionally, an integrated message passing interface (MPI) scheme is built to couple and resolve the communication between different scales in the model. The model results are then validated with experimental data and an automated workflow is established for model calculations without human intervention. Finally, a set of baseline operating conditions derived from the model simulation results is proposed to guarantee the production of high-quality thin-films.

© 2020 Elsevier Ltd. All rights reserved.

1. Introduction

In the semiconductor device fabrication, atomic layer deposition (ALD) is developed and utilized to enhance the deposition conformity in the high aspect ratio structures and to make the production of extremely-thin oxide films possible for the metal-oxide-semiconductor field-effect transistors (MOSFETs) (Schuegraf et al., 2013). To miniaturize the NAND (Not-And)-type flash memory devices with the pace of Moore's Law, companies and experimental labs have been constantly striving to reduce the dimension of the oxide films (e.g., SiO_2, Si_3O_4 and Al_2O_3) (Nalwa, 2002). However, the leakage current through the oxide film significantly increases due to quantum tunneling as the thickness of the traditional oxides becomes lower than 20 Å (Jeong et al., 2016). Further miniaturization is thus restricted by the lowering device reliability and the spiking power consumption. As a result, the endeavor of ensuring large electric potential barriers with a thin oxide film has been extensively investigated, and high dielectric constant (high-κ) materials are proposed as the solution (Ribes et al., 2005). Nevertheless, the surface deposition reactions of high-κ materials often have high activation energy barriers, thus leading to low-throughput, high operating costs and challenges for temperature sensitive material using ALD (Joo and Rossnagel, 2009). As an alternative to the high thermal energy, plasma-enhanced atomic layer deposition (PEALD) has been invented to overcome the high energy barrier, by benefiting from the high energy free radicals and ionic species (Won et al., 2005).

PEALD is a close variation of ALD. In a PEALD process, alternative pulses of neutral precursor and plasma-enhanced precursor are introduced to the reactor, with inert gas purge pulses in

* Corresponding author at: Department of Chemical and Biomolecular Engineering, University of California, Los Angeles, CA, 90095-1592, USA.
E-mail address: pdc@seas.ucla.edu (P.D. Christofides).

https://doi.org/10.1016/j.compchemeng.2020.107066
0098-1354/© 2020 Elsevier Ltd. All rights reserved.

between. Each precursor pulse is defined as a half-cycle, in which the associated precursor flows through the reactor, arrives at the substrate surface, and deposits the corresponding elements. Given appropriate operating conditions and sufficient precursor dosage, all the available reactive sites are occupied and reactions are completed in a self-limiting fashion. In the subsequent purge cycle, an inert gas is injected into the reactor, which removes the by-product and the left-over precursor gases to avoid undesirable reactions and multi-layer deposition (George, 2009). Following this approach, uniform high-κ dielectric thin-films can be rapidly deposited layer-by-layer in a well-controlled manner, and high operating temperatures and high energy consumption can be avoided (Ishikawa et al., 2017). In the last twenty years, there has been a large number of studies on new types of high-κ dielectric thin-film materials, novel plasma precursors, associated reaction mechanisms, and the design of plasma generators and reactor chambers. New oxide materials like TiO_2 (Kukli et al., 2000), HfO_2 (Liu et al., 2005), and ZrO_2 (Yun et al., 2004) are looked into because of their extraordinary gate capacitance, high thermal stability, good charge mobility, and the band alignment to the bottom silicon gates. Taking HfO_2 thin-film as an example, which has a dielectric constant 4–6 times higher than SiO_2, a variety of precursor combinations have been investigated. For the Hf half-cycle, Hf based metal-organic precursors are extensively studied, including tetrakis(dimethylamido) hafnium (TDMAHf) (Liu et al., 2003), tetrakis(ethylmethylamido) hafnium (TEMAHf) (Kukli et al., 2000), tetrakis(diethylamido) hafnium (TDEAHf) (Shi et al., 2011), etc. The H-N hydrogen bonds associated with these precursors lead to easier physisorption and dissociative chemisorption pathways and faster reaction rates. On the other hand, common plasma-enhanced oxide precursors include O_3 plasma (Rai et al., 2010), H_2O plasma (Kanomata et al., 2014), and O_2 (Rai et al., 2010) plasma. In addition, the reactor geometry is also critical to PEALD throughput and effectiveness. The nominal direct plasma reactor geometry is inherited from the thermal ALD chamber, where plasma is directly generated in the main reactor chamber right above the substrate. This simple reactor geometry allows for a small volume and fast flow-type operation but may result in damage of the substrate due to the high ionic energies in the plasma sheath (Won et al., 2014). To deal with this shortcoming, remote plasma and radical enhanced reactor configurations have been designed, in which plasma reaction happens at an appropriate remote distance, and ions are minimized while enough radicals are available to be transported to the substrate surface (Jeon et al., 2007). Thus, in this paper, we choose to investigate the deposition of HfO_2 thin-film using TDMAHf and oxygen plasma in a remote plasma reactor.

Despite the experimental efforts made to explore and understand the PEALD process, the high operating costs, the process complexity, and the lack of appropriate monitoring techniques restrict the exploration of a variety of operating conditions and the development of a comprehensive input-output relationship between operating parameters and film product properties. The hardware of PEALD is complicated and expensive, which involvesintricate chamber design and precise gas flow controllers. In the plasma generation chamber, a complex RF power source and sophisticated pumping systems are required (Lee et al., 2006; Profijt et al., 2011). In the main reactor, the influence of the complex gas-phase particle transport phenomena on the microscopic deposition profile has not been characterized (Zhang et al., 2020). On the wafer surface, the reaction details are also not fully understood, which is crucial to the deposition rate and the film property (Lee et al., 2006). The ability of the in-situ analysis techniques like quart crystal microbalance (QCM) and spectroscopic ellipsometry are limited (Pittal et al., 1993). Also, microstructure analysis methods like scanning tunneling microscopy (STM) and scanning electron microscope (SEM) are film destructive (Schwille et al., 2017). As a result, the accurate first-principles based modeling of the plasma reaction, macroscopic particle transport, and surface deposition is beneficial to both experimental and industrial work.

There have been many simulation models developed to capture the individual scale of the PEALD process. For the plasma reaction scale, Lee and Lieberman (1995) looked into a small set of representative reactions of O_2/Ar plasma. Tinck and Bogaerts (2011) simulated a combination of the remote inductively coupled plasma (ICP) oxygen plasma source and the species transport in a simplified reactor geometry. Corr et al. (2012) conducted a comparison between the experimental and simulation results of an O_2 ICP. For the gas-phase transport scale, commercial computational fluid dynamics (CFD) software have demonstrated their superior capabilities of accurately solving the gas-phase transport phenomena even for complex geometries (Gerogiorgis and Ydstie, 2005; Epelle and Gerogiorgis, 2017). Pan et al. (2014) simulated a cross-flow reactor for ALD of Al_2O_3. Crose et al. (2018) demonstrated a successful multiscale modeling of the plasma-enhanced chamber vapor deposition (PECVD) of amorphous silicon thin-films. Zhang et al. (2019) investigated a complex showerhead reactor for the thermal ALD of SiO_2. In addition, for the microscopic surface scale, the kinetic Monte Carlo (kMC) method is often utilized to model the thin-film deposition process, which achieves a decent computational efficiency and good model validity (Dkhissi et al., 2008; Elliott and Greer, 2004; Rey et al., 1991). Shirazi and Elliott (2014) investigated a complete set of reactions for a small scale simulation for HfO_2 ALD. Ding et al. (2019) used a tailored kMC to model the reaction competitions in the SiO_2 thin-film deposition using Bis(tertiary-butylamino)silane (BTBAS). More recently, Ding et al. (2020) adopted a similar methodology to model the surface reaction for HfO_2 using TDMAHf and oxygen plasma of an industrial wafer, which is the first step to construct a comprehensive model for PEALD as critical gas-phase transport and plasma considerations were not considered. At this point, there has not been any work that combines the three scales into one integrated framework for PEALD. To fully investigate and understand the complicated interactions between different components, it is really important to take a multiscale approach to interlink the important process dynamics together. Such a multiscale CFD model will provide substantial benefits by enabling a much more rigorous picture of the input-output relationship between operation conditions, gas-phase dynamics, and film surface details. Also, equipped with such a model, on-line optimization and even real-time control are made possible for PEALD as in a series of other multiscale processes (Chaffart and Ricardez-Sandoval, 2017, 2018, Kwon et al., 2015a, 2015b; Oh and Lee, 2016; Rasoulian and Ricardez-Sandoval, 2015, 2016; Wang et al., 2009).

In this paper, a multiscale CFD simulation of the PEALD process with TDMAHf and O_2 plasma as precursors is developed, with the first-principles thermodynamic parameters calculated from the density functional theory (DFT). Specifically, the multiscale model combines a 2D axisymmetric plasma reaction domain, a 3D macroscopic CFD domain for gas-phase transport, and a 3D microscopic kMC domain for surface deposition. In particular, the plasma reaction domain incorporates a 2D multi-physics model that accounts for the interaction of AC circuits, magnetic field, species transport, and ionic reactions for plasma generation simulation. Connected to the plasma boundary, a macroscopic gas-phase domain adopts a transient 3D CFD model to solve for the coupled species, momentum, energy transport, and the heavy particle reactions in the complex PEALD main reaction chamber. For the microscopic surface deposition domain, we adopt the previously developed 3D kMC algorithm by Ding et al. (2020) to capture the surface reaction mechanism and the structural details of the HfO_2 thin-film. DFT calculations are utilized to accurately characterize the key parameters of all domains, where thermal conductivity, viscosity, and heat capac-

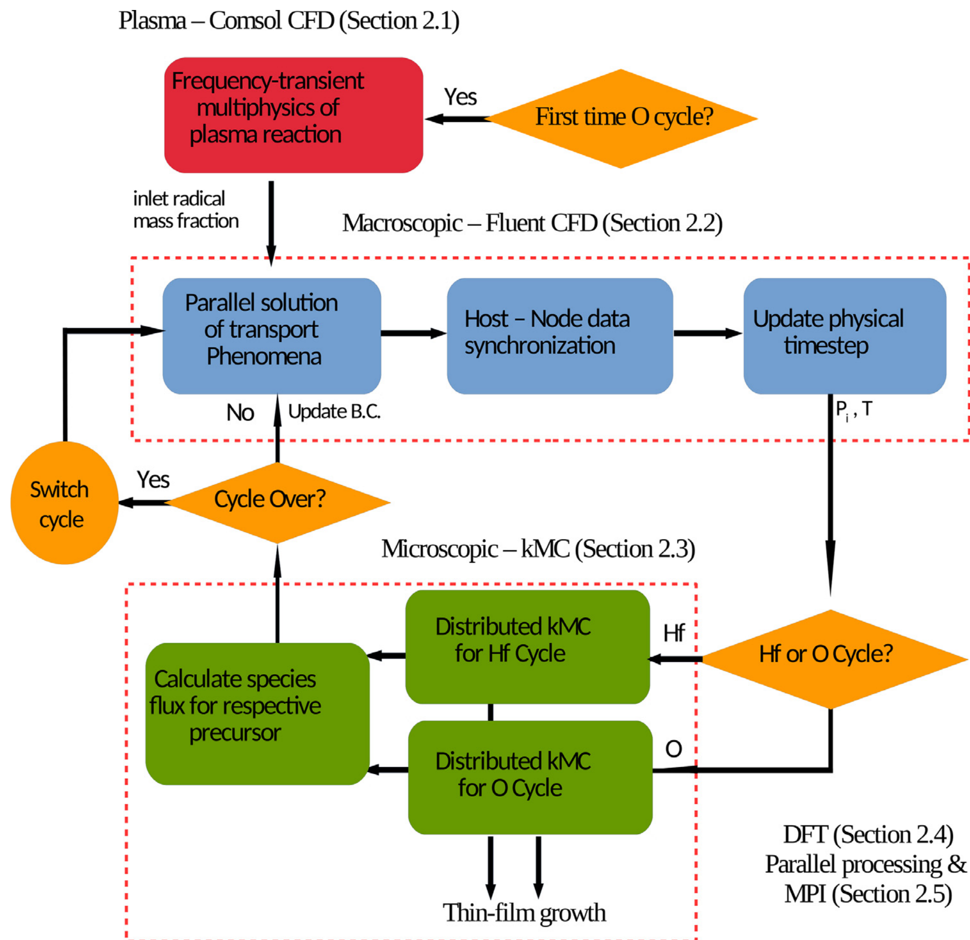

Fig. 1. Multiscale workflow, parallel processing and information exchange illustration.

ities affect the gas-phase CFD model, and the activation energies and surface structure detail are critical to the microscopic domain. Furthermore, to implement the coupling of three respective simulation models, a message passing interface (MPI) and parallel computation are used to link and solve all domains simultaneously.

2. PEALD process description and multiscale CFD modeling

This section addresses the construction of the 3D multiscale computational fluid dynamics (CFD) model that simulates the PEALD of HfO_2 thin-film. The workflow is shown in Fig. 1. First, the construction of the CFD model for the ICP plasma generation in the remote plasma chamber is explained in detail. Next, the gas-phase CFD model for transport phenomena in the main ALD reactor chamber is elaborated. After that, the previously developed kMC model for the microscopic surface film deposition is briefly reviewed. Finally, the information exchange through the automated workflow between the three models and the parallel computing architecture with the Message Passing Interface (MPI) scheme is presented.

2.1. Plasma chamber CFD model

The plasma chamber design and the tuning of operating parameters critically influence the plasma chemistry as well as the final substrate deposition. As discussed in Section 1, the remote plasma system has been commonly adopted in the recent industrial manufacturing processes. The remote plasma reactor design enhances the performance of thermal ALD with the high-energy radicals and avoids the surface damage caused by the direct ionic plasma sputtering on the substrate. Two kinds of plasma sources are often used: the capacitively coupled plasma (CCP) and the inductively coupled plasma (ICP). For PEALD application, the ICP plasma source, which generates plasma using the alternative current (AC) induced magnetic field, is often utilized due to its capability to deliver high density and high purity plasma. To simulate the coupled physics, we take advantage of the built-in plasma module in COMSOL Multiphysics software (Version 4.3). It is noteworthy that the plasma generation simulation is decoupled from the gas transport in the main reactor chamber due to the difference in model timescales. Specifically, compared to the transport timescale in the main reactor chamber, which is typically around a couple of seconds, the timescale associated with plasma generation is extremely short, which is typically around 10^{-3} s. Therefore, it is reasonable to neglect the interaction between the plasma generation and the subsequent reactor transport. The simulation geometry we select is the Gaseous Electronics Conference (GEC) cell, which was introduced by the National Institute of Standards and Technology (NIST) at the 1988 GEC projects, aiming at providing a standard experimental and modeling platform for electronic and plasma study. The outlet is modified to fit the connection to the reactor main body, which is shown in Fig. 2.

For the ICP power source, the power of AC generator is set to 2000 W, and the current flows through the five fold copper coil at a radio-frequency (RF) of 13.56 MHz. The AC current creates a changing electric field $\vec{E}$ and a changing current density $\vec{J}$, which lead to the generation of the magnetic field given by the Ampere-

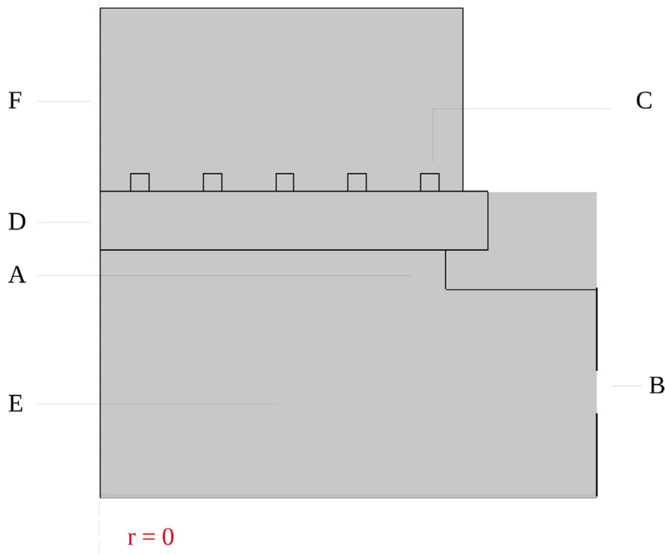

Fig. 2. Axis-symmetric geometry of the plasma reaction chamber. The gas inlet is labeled as A, the gas outlet is labeled as B, the coil circuits are labeled as C, the circuit wall, which is made of quartz, is labeled as D, the reaction chamber is labeled as E, and the relevant ambient atmosphere region is label as F. The red dashed line on the left is the symmetry axis. Note that exit is only one side of the reactor. (For interpretation of the references to colour in this figure legend, the reader is referred to the web version of this article.)

Maxwell equation:

$$\vec{\nabla}(\epsilon_f \vec{B}) = \vec{J} + \epsilon_0 \frac{\partial \vec{E}}{\partial t} \quad (1)$$

where ϵ_f is the electric permeability of materials, $\vec{B}$ is the magnetic field, ϵ_0 is electric permeability of free space and t is the time.

The plasma chamber is constantly filled with argon, and when the oxygen cycle is about to start, the oxygen valve is opened to introduce an oxygen flow and the AC circuit is activated. The Ar/O_2 plasma generation is governed by the reaction sets shown in Table 1, Table 2 and Table 3. Three types of reactions are defined and simulated in COMSOL: the electron impact reactions, which involve the participation of electrons, the heavy particle reactions, which involve only atomic and molecular species, and the surface reactions, which occur at the plasma chamber surfaces. The electron impact reactions are further classified into four categories including elastic, ionization, excitation, and attachment reactions, and their rates can be accurately captured by the reaction collisional cross-section data. Heavy particle reactions include charge exchange, recombination, and quenching and the rates of heavy particle reactions can be characterized by Arrhenius-type equations using appropriate rate constants. In addition, the rates of surface reactions can be computed by the sticking coefficients on the wall-surface material. The important reaction parameters, collisional cross-section data and sticking coefficients can be found in Lee and Lieberman (1995), Tinck and Bogaerts (2011) and COMSOL documentations (Multiphysics, 1998). The species involved in the reactions include: $O(^3P)$, or O, which is the ground state atomic oxygen; $O(^1S)$, which is the first excited atomic oxygen; $O(^1D)$, which is the second excited atomic oxygen; $O_2(^3\Sigma_g^-)$, or O_2, which is the ground state molecular oxygen; $O_2(^1\Delta_g)$, which is the first excited singlet molecular oxygen; $O_2(^1\Sigma_g^+)$, which is the second excited singlet molecular oxygen; Ar, which is the ground state argon, and Ar^*, which is the excited argon. For ionic species, $^-$ and $^+$ refer to the negative and positive charges respectively. Finally, e stands for the electron.

Table 1
Heavy particle and electron impact reactions.

Reaction	Formula	Type
1	$e + O_2 => e + O_2$	Elastic
2	$e + O_2 => O + O^-$	Ionization
3	$e + O_2 => e + O_2(^1\Delta_g)$	Excitation
4	$e + O_2 => e + O_2(^1\Sigma_g^+)$	Excitation
5	$e + O_2 => e + 2O$	Excitation
6	$e + O_2 => e + O + O(^1D)$	Excitation
7	$e + O_2 => e + O + O(^1S)$	Excitation
8	$e + O_2 => 2e + O_2^+$	Ionization
9	$e + O_2(^1\Delta_g) => e + O_2(^1\Delta_g)$	Elastic
10	$e + O_2(^1\Delta_g) => e + 2O$	Excitation
11	$e + O_2(^1\Delta_g) => 2e + O_2^+$	Ionization
12	$e + O_2(^1\Sigma_g^+) => e + O_2(^1\Sigma_g^+)$	Elastic
13	$e + O_2(^1\Sigma_g^+) => e + 2O$	Excitation
14	$e + O_2(^1\Sigma_g^+) => 2e + O_2^+$	Ionization
15	$e + O => e + O$	Elastic
16	$e + O => e + O(^1D)$	Excitation
17	$e + O => e + O(^1S)$	Excitation
18	$e + O => 2e + O^+$	Ionization
19	$e + O(^1D) => e + O(^1S)$	Excitation
20	$e + O(^1D) => 2e + O^+$	Ionization
21	$e + O(^1S) => 2e + O^+$	Ionization
22	$e + Ar => e + Ar$	Elastic
23	$e + Ar => e + Ar^*$	Excitation
24	$e + Ar => 2e + Ar^+$	Ionization
25	$e + Ar^* => 2e + Ar^+$	Ionization
26	$e + O_2 + O_2 => O_2 + O_2^-$	Attachment
27	$e + O_2^+ => 2O$	Attachment
28	$e + O_2^+ => O + O(^1D)$	Attachment

Table 2
Heavy particle reactions.

Reaction	Formula	Type
1	$O_2(^1\Delta_g) + O_2 => O_2 + O_2$	Quenching
2	$O_2(^1\Delta_g) + O => O_2 + O$	Quenching
3	$O_2(^1\Delta_g) + O(^1D) => O_2 + O$	Quenching
4	$O_2(^1\Delta_g) + O_2(^1\Delta_g) => O_2 + O_2(^1\Sigma_g^+)$	Quenching
5	$O_2(^1\Sigma_g^+) + O_2 => O_2 + O_2$	Quenching
6	$O_2(^1\Sigma_g^+) + O_2 => O_2(^1\Delta_g) + O_2$	Quenching
7	$O_2(^1\Sigma_g^+) + O => O_2 + O$	Quenching
8	$O_2(^1\Sigma_g^+) + O => O_2 + O(^1D)$	Quenching
9	$O(^1D) + O_2 => O + O_2$	Quenching
10	$O(^1D) + O => 2O$	Quenching
11	$O(^1D) + O_2 => O_2(^1\Sigma_g^+) + O$	Quenching
12	$O(^1D) + O_2 => O_2(^1\Delta_g) + O$	Quenching
13	$O(^1S) + O_2 => O + O_2$	Quenching
14	$O(^1S) + O => 2O$	Quenching
15	$2O + O_2 => 2O_2$	Recombination
16	$3O => O + O_2$	Recombination
17	$O^+ + O_2 => O + O_2^+$	Charge exchange
18	$O^- + O => O_2 + e$	Ionization
19	$O^- + O_2 => O + O_2^-$	Charge exchange
20	$O^- + O^+ => 2O$	Recombination
21	$O^- + O_2^+ => 3O$	Recombination
22	$O^- + O_2^+ => O_2 + O$	Recombination
23	$O_2^- + O_2^+ => 2O2$	Recombination
24	$O^- + Ar^+ => O + Ar$	Recombination
25	$O_2 + Ar^* => O_2 + Ar$	Quenching
26	$O_2 + Ar^* => 2O + Ar$	Quenching
27	$O_2 + Ar^+ => O_2^+ + Ar$	Charge exchange
28	$O + Ar^* => O + Ar$	Quenching
29	$O + Ar^+ => O^+ + Ar$	Charge exchange

To simulate the interaction of the physical processes, we combine the simulation of fluid flow (laminar flow module), heat transfer (heat transfer in fluid), magnetic field (AC/DC module), and plasma reaction (plasma reaction) together with COMSOL Multiphysics function. A frequency-transient model is selected to investigate the plasma reaction and generation, which outputs the ion and radical compositions throughout the plasma chamber. Because of the comparatively fast development time compared to the

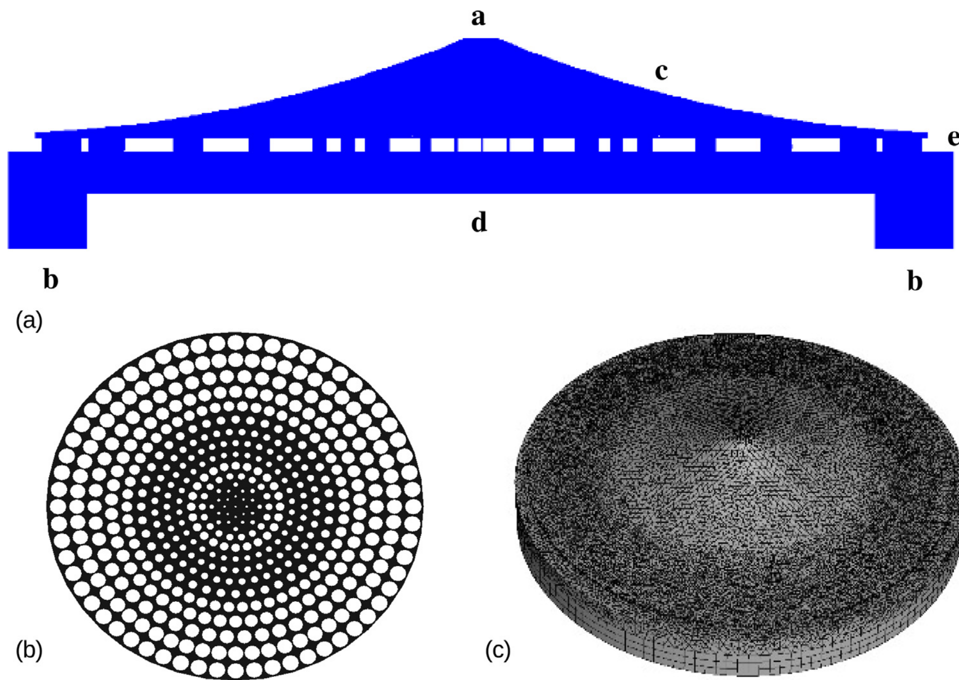

Fig. 3. Reactor *y* cross-section view, showerhead design and hybrid mesh. The precursor/plasma inlet is labeled **a** and the outlet is labeled as **b**. The reactor upstream is labeled **c**, where the gas-profile develops. The substrate surface is labeled **d**. The showerhead panel is labeled **e**.

Table 3
Surface plasma reactions.

Reaction	Formula	Type
1	$O_2(^1\Delta_g)$ => O_2	Surface
2	$O_2(^1\Sigma_g^+)$ => O_2	Surface
4	O_2^+ => O_2	Surface
5	$O(^1D)$ => O	Surface
6	$O(^1S)$ => O	Surface
7	O^+ => O	Surface
8	2O => O_2	Surface
9	Ar^+ => Ar	Surface
10	Ar^* => Ar	Surface

Table 4
Cell quality of the hybrid reactor mesh (* symbolizes the desired value).

	Acceptable Range	Bound; Average
quality	0 - 1*	0.14; 0.82
skewness	0* - 0.95	0.87; 0.24
aspect ratio	1* - 100	1.85; 1.12

species transport, a steady-state profile can be chosen as the constant output for the inlet profile of the subsequent domain.

2.2. Macroscopic CFD model

The surface deposition profile of the HfO_2 thin-films is closely related to the gas-phase species transport in the main reactor chamber. In this work, we build a 3D ALD reactor model and use ANSYS Fluent 2019R3, a commercial CFD software, to solve for the coupled energy, momentum, and mass transport phenomena. The reactor geometry design, the meshing, and the CFD model details are discussed in the following sections.

2.2.1. Reactor design and meshing

There are a variety of ALD reactor designs developed by the semiconductor manufacturing companies. In this work, we adopt the ALD reactor design developed in Zhang et al. (2019), which is originally based on the EmerALD XP by ASM International (Lee et al., 2006). Specifically, the reactor chamber design is optimized to achieve a uniform gas transport profile and is scaled to accommodate the commercial 300-mm diameter wafer, which is shown in Fig. 3(a) (King, 2011). Precursor gases (both hafnium precursor and oxygen plasma) are introduced from the top of the reactor through a 1-cm diameter inlet with the argon carrier gas, and the gas-profile is first developed in the upstream region, which features a horn-shaped design to allow fast and uniform gas distribution. Then, the gas stream flows downward and the downstream gas-profile is tested either with or without a showerhead panel, which contains optimized hole sizes and hole distribution, as shown in Fig. 3(b). Finally, the gas stream uniformly approaches and reacts with the substrate surface, and the unreacted precursor and carrier gas exit from the bottom outlet, which has an inner and outer diameter of 30 cm and 36 cm, respectively.

Moreover, in order to utilize the geometry for CFD computation, a fine mesh needs to be generated for the reactor geometry, where the reactor domain is dissected into geometric primitives. Adopting the hybrid meshing technique developed in Zhang et al. (2019), the reactor geometry is decomposed into two zones using structured and unstructured meshes, respectively. As a result, a good overall cell quality can be guaranteed, and the number of cells can be minimized. To balance the computation efficiency and accuracy, as shown in Fig. 3(c), a final mesh of around 1.2 million cells is determined to be adequate from the mesh independence test, where respective quality metrics are shown in Table 4. The results show that the quality of all cells lie within the acceptable quality range and each average metric is close to the optimal values suggested by the Fluent manual (Fluent, 2013).

2.2.2. Gas-phase transport model

In this section, the simulation setup in the main reactor gas chamber using ANSYS Fluent is discussed in detail. A pressure-based solver is utilized, which is appropriate for low pressure and near-room temperature systems. Twelve gas-phase species are incorporated in the model: argon is used as carrier and purging

gas; TDMAHf is the Hf-cycle precursor; ground state molecular oxygen and atomic oxygen, together with their excited and ionic states, are the O-cycle precursors, as specified in the last section. The by-products from the surface reactions are ignored because of the limited contribution to the fluid flow from the relatively small quantities being generated. While the thermodynamics and kinetics properties of the oxygen-related species and argon can be found in the Fluent Database, TDMAHf is defined using literature and previously obtained values from density functional theory (DFT) (Jeon and Won, 2008; Shirazi and Elliott, 2014; Ding et al., 2020). The molecular weight of TDMAHf equals 354.8 g/mol, while its heat capacity, viscosity, and thermal conductivity are defined with linear temperature dependency, which will be discussed in further detail in Subsection 2.4. A base operating pressure is set to be 60 Pa, which is achieved with constant pumping and a flow of 300 sccm Ar. The operating pressure in each half cycle may increase because of the additional precursor in each cycle. The chosen operating pressure is within the general pressure range of 100 to 500 mTorr for typical PEALD and ALD processes (Lao et al., 2005; George, 2009). In addition, CFD boundary conditions are defined according to the PEALD operations from experimental works (Heil et al., 2007). The profile of the reactor inlet is defined using several user-defined functions (UDF) in Fluent, which characterize the inlet flow rates, temperature, the duration of each half-cycle and purging steps, and species mass fluxes. In particular, the inlet is defined with the equivalent profile of a gas-delivery bubbler at 348.15 K, which is a typical temperature that leads to the vapor pressure of 1 Torr for the TDMAHf (Hausmann et al., 2002). The outlet is also defined with UDF, which simulates a 12 m^3/h vacuum pump to drive the existing pressure to be 1×10^{-6} mTorr in the actual reactor outlet (Joo and Rossnagel, 2009). The substrate surface is the interface between the microscopic and macroscopic domains. UDFs are again adopted to gather gas-phase surface temperature and pressure information that is used by the microscopic model and also to define the boundary conditions for the substrate surface, which accounts for the precursor consumption rate and surface temperature. In addition, both volumetric and surface reaction sets are defined. For most surface reactions, shown in Table 3, a sticking coefficient of 1 and a high rate constant is used in the Arrhenius equation to simulate the instantaneous de-excitation and de-ionization. For atomic oxygen recombination, a sticking coefficient of 0.17, reported in Tinck and Bogaerts (2011), is simulated using the source UDF. For plasma reactions, only heavy particle reactions, as shown in Table 2, are included in the gas-phase model as the number density of electrons is negligible due to the long distance from the remote plasma chamber to the main reactor chamber.

With the appropriate boundary conditions applied on the inlet, outlet and the substrate surface, reaction kinetics and the momentum, mass, and energy transport equations are solved to obtain the gas-phase velocity, concentration, and temperature profile. Surface temperature and pressure within the boundary layer can be extracted from the computed gas-phase profile, and provide information for the microscopic computation. To effectively solve the Navier-Stoke equations and other transport equations simultaneously, the coupled solver in ANSYS Fluent is used. The following flow field and reaction rate equations, shown in the tensor form, are solved in each time step (Fluent, 2013):

$$\frac{\partial}{\partial t}(\rho E) + \nabla(\vec{v}(\rho E + P)) = \nabla(k\nabla T - \Sigma h\vec{J} + (\bar{\bar{\tau}}\vec{v})) + S_h \tag{2}$$

$$\frac{\partial(\rho\vec{v})}{\partial t} + \nabla\cdot(\rho\vec{v}\,\vec{v}) = -\nabla P + \nabla\cdot\left(\bar{\bar{\tau}}\right) + \rho\vec{g} + \vec{F} \tag{3}$$

$$\bar{\bar{\tau}} = \mu\left[\left(\nabla\vec{v} + \nabla\vec{v}^{T}\right) - \frac{2}{3}\nabla\cdot\vec{v}I\right] \tag{4}$$

$$\frac{\partial}{\partial t}(\rho Y_i) + \nabla\cdot(\rho\vec{v}Y_i) = -\nabla\cdot\vec{J_i} + R_i + S_i \tag{5}$$

$$\vec{J_i} = -\rho D_{m,i}\nabla Y_i - D_{T,i}\frac{\nabla T}{T} \tag{6}$$

$$\vec{R_i} = M_{w,i}\sum_{r=1}^{N_r} R_{i,r} \tag{7}$$

where ρ is the density of the gas-phase species mixture, E is the fluid internal energy, $\vec{v}$ is the velocity of gas-phase species mixture, P is the static pressure, k is the thermal conductivity, T is the fluid temperature, $\bar{\bar{\tau}}$ is the stress tensor, h is the sensible enthalpy $\vec{J}$ is the mixture diffusion flux, S_h is heat transfer source term, $\vec{g}$ is the component of gravity on the direction of the fluid flow, F is the external force, μ is the fluid viscosity, I is the unit tensor, Y_i is the mass fraction of species i, $\vec{J}$ is the diffusive flux, R and S are the reactions and mass transfer source terms, respectively, and D_m and D_T are the mass and heat diffusivities. For the total reaction rate $\vec{R}$, M_w is the molecular weight, N_R is the number of reactions involved for the species, and R_r is the individual rate of generation/consumption, which is governed by the rate constant specified in the UDFs. For all the above variables, subscript i refers to species i.

Based on the mesh developed in the previous section, the finite volume method is utilized by ANSYS Fluent to implicitly solve the aforementioned equations (Eymard et al., 2000). Specifically, at each time step, calculations for all transport equations are iterated until all residual convergence conditions satisfy the respective predefined criterion. The chosen calculation time step is also critical to the CFD simulation efficiency and accuracy (Courant et al., 1967). According to the Courant-Friedrichs-Lewy (CFL) condition, a criterion on finite-difference approximation of PDEs, the time step size can be related to the spatial interval lengths Δx, the information traveling speed u, and the Courant number C, which is the number of computational cells that the fluid information can pass through in each time step, (Moura and Kubrusly, 2012):

$$\Delta t = \frac{C\Delta x}{u} \tag{8}$$

Advanced CFD software allows convergence under higher courant number for faster CFD computation (Moura and Kubrusly, 2012). In particular, a courant number of 50 is used in our pressure-based solver to efficiently arrive at an accurate solution. According to Eq. (8), the appropriate time step sizes can be determined for each half cycle and the purging steps based on the different gas flow velocities.

2.3. Microscopic surface model

In addition to the plasma chamber and the gas-phase transport through the main reactor, the reactions on the substrate surface need to be characterized. Utilizing a previously determined 3D kMC algorithm, the surface deposition model describes the detail structure of the HfO_2 thin-film and the important reaction mechanisms. The assumed 3D lattice, reaction kinetics and pathway of the surface physical and chemical reactions, and the kMC algorithm are developed in Ding et al. (2020) and discussed in the following subsections.

2.3.1. Structural characterization of the deposited HfO_2

HfO_2 takes on a variety of crystal lattice structures, depending on the substrate temperature. At a low operating temperature of the PEALD, the monoclinic phase alike structure is considered in the model (Kumar et al., 2017), as shown in Fig. 4(a). For the starting surface, the (111) direction is considered, and surface treatments using piranha solution and dilute HF solution

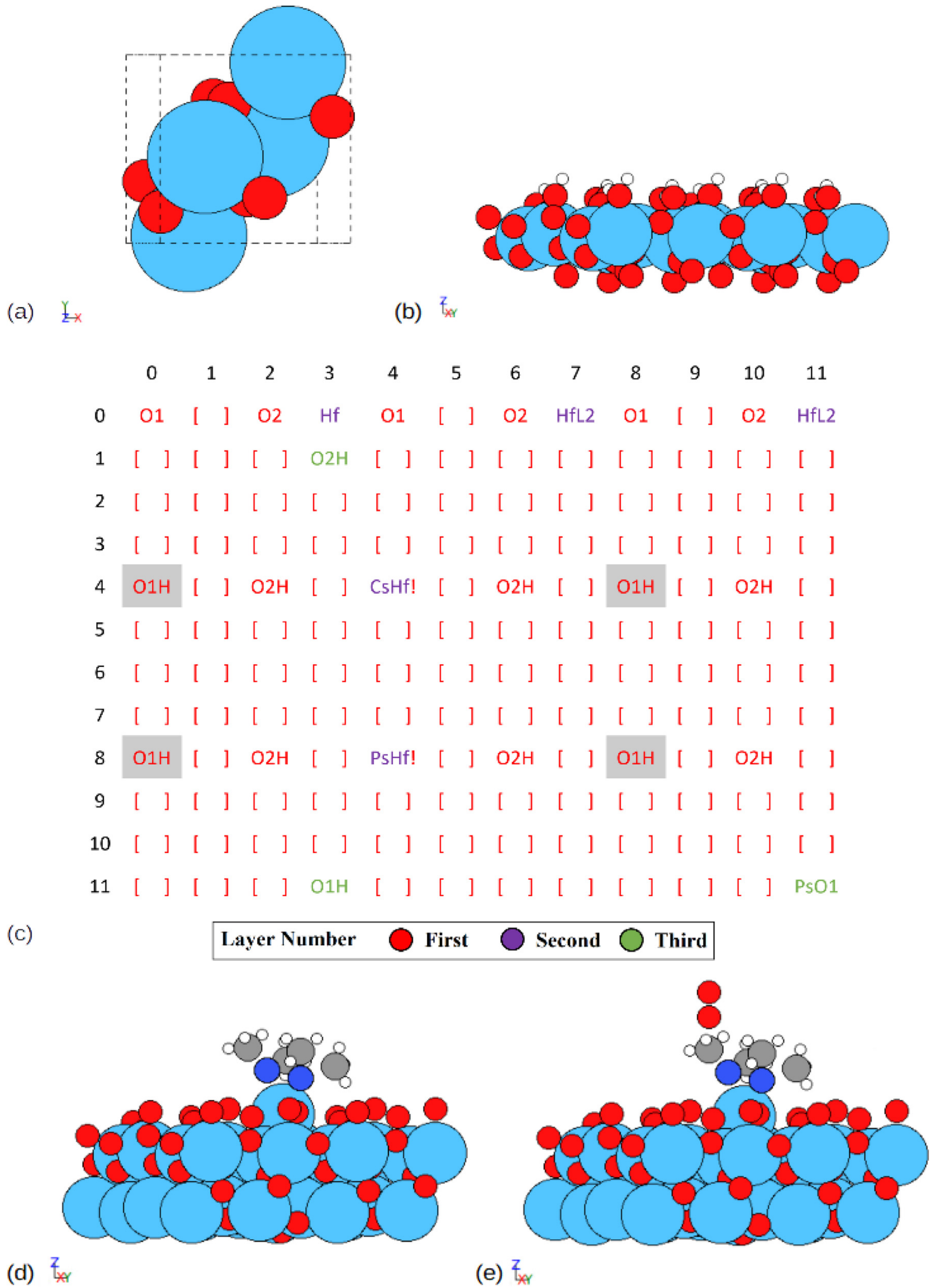

Fig. 4. Surface slab and approximated lattice. (a) The HfO_2 unit cell. (b) The clean hydroxyl-terminated HfO_2 slab. (c) The approximated lattice used in the simulation. (d), (e) The HfL2-terminated slab with and without O_2 physisorption, respectively. (For interpretation of the references to colour in this figure legend, the reader is referred to the web version of this article.)

leads to a clean hydroxyl-terminated configuration, as shown in Fig. 4(b). In order to reduce the computational and conceptual complexity, the 3D triangular on-lattice approximation developed in Ding et al. (2019) is adopted, and it assumes the Hf-O-Hf bond angleto be 90 degree, which successfully preserves the important structural features. An example of the resulting simulation lattice is shown in Fig. 4(c), which contains exemplary icons of most of the associated species. PsHf represents the physisorbed precursor, CsHf represents the chemisorbed precursors, HfL2 represents the deposited Hf terminated with two methylamino ligands, and PsO1 and PsO2 represent two distinct physisorbed oxygens. We can see that this approximated lattice resembles the real lattice structure and gives rise to a realistic cycle repetition pattern. In order to be size-independent, the simulation lattice is determined to be 1200 × 1200 × (the number of cycles simulated) (Huang et al., 2010).

2.3.2. Reaction mechanism

During each half cycle, the associated precursors transported from the macroscopic reactor scale will react and deposit the desired layer of element onto the film. For the Hf half-cycle, TDMAHf remains the precursor, and for the O half-cycle, atomic oxygen, oxygen gas, and their radicals are the major reaction species, as demonstrated in the result of the macroscopic scale simulation. A key reaction set was selected from the detailed mechanism reported in Shirazi and Elliott (2014) and Jeon and Won (2008), with simplifications on the proton diffusion, ligand rotation, and other features, which dramatically reduce the computational demand, making industrial-sized wafer-scale simulation feasible while preserving the reaction mechanism fidelity. The reaction mechanisms are shown in the Fig. 5, where the black arrows denote the reaction pathways, and the red arrows denote possible proton diffusion, where *Hs* denote the possible protons.

In the Hf-cycle, the reaction set contains physisorption, two-step dissociative chemisorptions, and desorption, which is shown in Fig. 5(a). The precursor (TDMAHf) particles that are in contact with the hydroxyl-terminated surface first physisorb onto the more electronegative hydroxyl group, as shown in Fig. 5(1). Subsequently, the precursor goes through the first chemisorption step, where the hydrogen atom from the attacked hydroxyl group is transferred to the precursor and release a dimethylamine (DMA) group, as indicated by Fig. 5(2). Next, as indicated by Fig. 5(3), another DMA group is released after reacting with the neighbor hydroxyl group, anchoring the hafnium atom onto the substrate surface. The resulting slab is terminated by the remaining two DMA groups, and the surface terminal species transfer back some of the ligand protons to the neighbor sites.

In the O-Cycle, both the ground state particles and their radicals have an important contribution to the deposition rate as demonstrated in our previous work and in experimental studies (Provine et al., 2016). The high energy of radicals, $^1O_2$ and ^3O, easily overcome the energy barrier, thereby instantaneously oxidizing the surface DMA groups and generating ethanimine compounds or the nitroxyl and ethane as byproducts as shown in Fig. 5(4) and Fig. 5(5). For the neutral species, $^3O_2$, the competition of the surface reactions is important to be characterized. First, the $^3O_2$ is physisorbed on to the substrate as a ring-shaped complex with the terminating DMA, as shown in Fig. 5(6). This physisorbed complex may desorb from the surface, as shown in Fig. 5(7), or move forward and oxidize, producing nitroxyl and ethane as byproducts in each step and eventually regenerates the OH-terminated slab, as shown in Fig. 5(8).

2.3.3. Relative rate determination and kinetic monte-carlo algorithm

The reaction kinetics of the pathways discussed in the previous section is crucial to the kinetic Monte-Carlo (kMC) method. Two ways of computing reaction rates are typically adopted to characterize the reactions involved in our model. The dissociative chemisorption, oxidation and desorption are thermodynamically activated reactions, which can be described by the general Arrenhius-type equation from the transition state theory (TST) as follows (Cortright and Dumesic, 2001):

$$r_{rxn} = A\exp\left(\frac{-E_a}{RT}\right) \tag{9}$$

where E_a is the activation energy of the transition state complex, A is the pre-exponential factor, R is the gas constant, and T is the substrate temperature.

In contrast, collision theory can be used to describe the gas-surface athermal barrierless processes like physisorption r_{phs}, which is governed by the partial pressure p of the precursor:

$$r_{phs} = \frac{p}{RT}\sqrt{\frac{8RT}{\pi m}} s_c N_a \sigma \tag{10}$$

where m is the molar weight of the precursor, R is the gas constant, σ is the unit cell surface area, N_a is the Avogadro number, and s_c is the sticking coefficient, reported in Dorsmann and Kleijn (2007).

The modified n-fold hybrid kMC algorithm, developed in (Ding et al., 2019), is applied to determine the reaction selection and time evolution to simulate the deposition profile and the structural growth, which is dependent on the total reaction rate r_{total}:

$$r_{total} = \sum_{i=1}^{N} r_i \tag{11}$$

where r_i represents the respective rate of each event within a N events set. For the event selection, a random number $\gamma_1 \in (0, 1]$ is used to locate the event according to its normalized indicator, $l_i \in (0, 1]$, which is defined as the sum of the normalized probabilities of the previous events:

$$l_i = \frac{\sum_{j=1}^{i} r_{unweighted}^{j} C_j}{\sum_{k=1}^{N} r_{unweighted}^{k} C_k}, \quad i = 1, \ldots, N \tag{12}$$

where the reaction rate $r_{unweighted}$ will be adjusted with respect to the available reacting agents for each event C, which is explained in detail in Ding et al. (2020). The i-*th* event is chosen for execution if the random number lies in between l_{i-1} to l_i.

The time evolution is calculated using a second random number $\gamma_2 \in (0, 1]$:

$$\Delta t = \frac{-\ln \gamma_2}{r_{total}} \tag{13}$$

The event times are added to the simulation time clock until the predefined half-cycle time is reached.

2.4. DFT and thermodynamic calculations

In order to correctly implement the proposed first-principles based method, many fundamental thermodynamic properties of TDMAHf need to be captured for the microscopic kMC model and the macroscopic CFD model. Thus Density functional theory (DFT) calculations are adopted using Gaussian09 software packages and molecular visualization toolbox ASE (Frisch et al., 2000; Liu and Liu, 2018). DFT is a solution to the Schrödinger equation, which calculates the electron density by approximating an exchange-correlation functional for the ground state energy of the system.

For the macroscopic model, TMDAHf is not defined in the Fluent material database, and the majority of the physical and chemical properties are not reported in previous works, including the thermal conductivity k, the specific heat C_p, and the viscosity

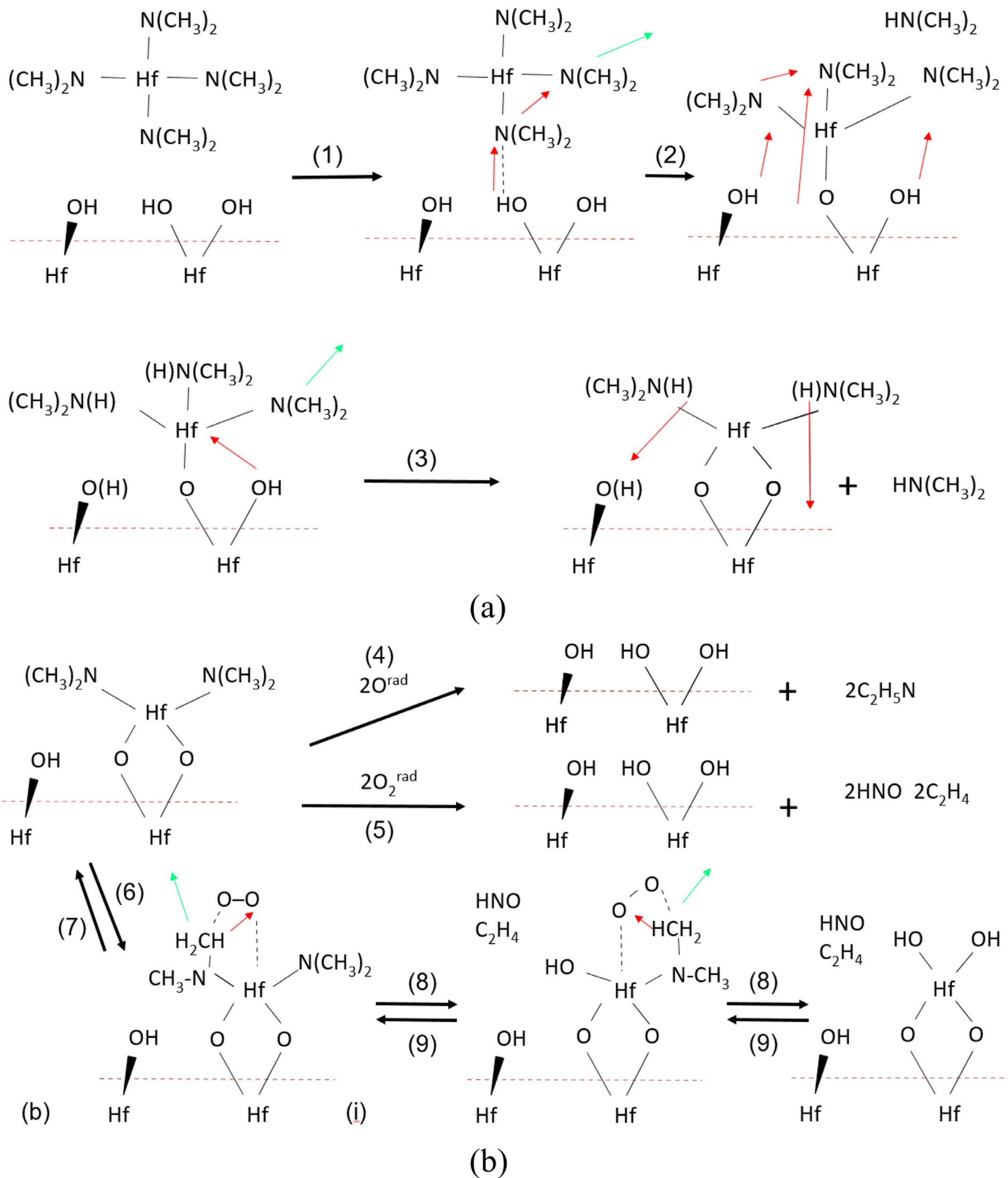

Fig. 5. Illustration of precursor surface reaction mechanisms.

μ. To estimate those parameters, the Hartree-Fock (HF) method is adopted with the Los Alamos National Laboratory 2-double-z (LanL2DZ) basis, which is a reasonable basis set for atoms like Hf considering the accuracy and computational speed (Check et al., 2001). Specific heat C_p is directly given by the DFT calculation, while viscosity μ can be calculated according to the molecular theory of Newtonian gas (Bird et al., 2007):

$$\mu = \frac{2}{3\pi} \frac{\sqrt{\pi m k_b T}}{\pi d^2} \tag{14}$$

where k_b is the Boltzmann constant, m is the molecular mass, d is the rigid ball diameter of TDMAHf molecule, and T is the absolute temperature. In addition, thermal conductivity k is calculated with the Chapman-Enskog relation (Garcia and Alder, 1998):

$$k = f \mu C v \tag{15}$$

where f is the correlation constant that has the value of 2.5.

For the microscopic model, the desorption rate of oxygen gas is an important factor that influences the neutral specie contribution to the deposition, which is investigated in our microscopic modeling investigation (Ding et al., 2020). A single-Hf(NCH_3)$_2$-terminated HfO_2 slab is created using python Catkit package and optimized using CatGen as shown in Fig. 4(d). The molecular oxygen gas is then positioned onto the terminating -NCH_3 group to mimic O_2

desorption, as shown in Fig. 4(e). Adopting the transition state calculation, the resulting slab is optimized for an initial guess of the configuration and the activation energy of the desorption reaction can be further obtained using the trial-and-error method (Hay and Wadt, 1985a; 1985b; Wadt and Hay, 1985).

2.5. Automated workflow and parallelization

It is not only important to ensure the successful simulation of each scale, but also to make sure the connections between all domains are effective and accurate. The automated workflow, shown in Fig. 1, provides an overview of how the solution of each domain is relayed in this work. The blue region represents the gas-phase domain (macroscopic), the green region represents the surface deposition domain (microscopic), the red region represents the plasma generation domain, and the arrows and the yellow region represent the cross-linkage through the message passing interface (MPI). The simulation starts at the hafnium half-cycle (Hf-Cycle), during which the plasma generation simulation is not triggered. The macroscopic model in Fluent starts to solve for the mass and energy balances of TDMAHf and Ar for a prescribed time step Δt. The substrate surface is dissected into 36 sub-regions, and the surface temperature and partial pressure conditions are collected for each sub-region. These information on surface temperature and pressure is then transferred to the microscopic domain. Under each sub-region in the microscopic domain, a microscopic kMC model will be triggered to perform the surface reaction simulation and determine the evolution of surface structure within the given interval Δt. After the kMC computations are completed and synchronized, the precursor consumption information will be used to calculate the species flux for each of the sub-region and reported back to the macroscopic domain. Next, system simulation clock will be advanced to $t + \Delta t$, and the boundary conditions of the macroscopic model will be updated according to calculated fluxes (Fluent, 2013). The above steps are repeated until the end of the Hf-cycle, and the time selection scheme will switch the conditions to the subsequent purge cycle, where residual TDMAHf can potentially continue the physisorption until purged out of the reactor. During the oxygen half-cycle (O-Cycle), before the execution of the gas-phase CFD model, the plasma generation model in COMSOL will be triggered to calculate the plasma reactions and to provide the inlet information (e.g., mass fraction plasma species and temperature) for Fluent, which is used in all subsequent O-Cycles. Also, the volumetric and surface reaction will be turned on in Fluent for the gas-phase CFD model during O-Cycles. The overall workflow will be iterated until the predefined cycle number has been arrived.

To enhance the computational efficiency, job distribution and parallelization are realized for the PEALD microscopic and macroscopic domain calculation, respectively. For the macroscopic domain, because of the high computational demand of the fine mesh and the volumetric reactions, 84 computing cores each equipped with 8 GB or 16 GB RAM on the UCLA hoffman2 cluster are used. The number of used cores is based on the resource available on the cluster, the communication overhead, and the parallel computing benchmark. The job parallelization is managed using the Fluent Message Passing Interface (MPI) (Fluent, 2013). On the other hand, the local microscopic kMC models are distributed onto the idle computing cores, where 36 kMC models run simultaneously and the results are gathered and synchronized.

3. Multiscale CFD simulation results and operating condition exploration

In this section, we validate the performance of the constructed CFD model by first comparing each component of the multiscale model (the plasma generation, the main chamber gas-phase transport, and the microscopic deposition) with experimental observations and individual scale simulations. Then, the collective influence of plasma generation and gas-phase transport on the deposition of the substrate will be investigated.

3.1. Plasma generation

The plasma generation model in the RF excited remote plasma chamber is tested with an inlet volumetric flow rate of 100 sccm of Ar and O_2 mixture, in which Ar has a mole fraction of 0.3 and O_2 has a mole fraction of 0.7. The coil has a power of 2000 W and the plasma chamber pressure is set to be 2.67 Pa. Using a frequency-transient simulation, steady-state can be reached at 3×10^{-4} s, which is demonstrated to be much faster than the gas-phase transport as discussed in the Section 2.1. The spatial distributions of the electron and species densities at steady-state are shown in Fig. 6.

The power distribution inside the plasma chamber is demonstrated to have its maximum value close to the coils. The resulting electron number density is in the range of 10^{17} $1 \cdot m^{-3}$, which is close to the value reported in Tinck and Bogaerts (2011) and Lee et al. (1994) at similar operating pressure and power, and the exact values differ because of the chamber geometry and coil layout. Also, as shown in Fig. 6(b), we can see that the maximum electron density lies at the center of the generation chamber as expected. Due to the larger reactor geometry and the horizontally distributed coils simulated in this work, the power used in this model is higher than in some other research works. For example, a power of 1000 W, leading to a capacitive power deposition of 0.1 - 1 W/m^3 was reported by Lee et al. (1994). Whereas in our model, a power of 2000 W is used, leading to a capacitive power deposition of 1.6 W/m^3. It is demonstrated that at higher power, the gas heating is more significant, which leads to a higher electron temperature, T_e. On the other hand, the electron temperature decreases with a higher chamber pressure as observed in Lee et al. (1994). Thus, with a reasonable extrapolation based on the trend of power, we can estimate that the expected electron temperature lies in the range of 2 - 5 V, which successfully correlates the result observed in our simulation model, as shown in Fig. 6(a).

The number densities of O_2 and its excited species are shown in Fig. 6(h) and (g). For O_2, the maximum number density is at the inlet and the majority of O_2 are excited at the center of the reactor to the activated species: $O_2(^1\Delta_g)$ and $O_2(^1\Sigma_g^+)$. Away from the center, O_2 reappears from the recombination of atomic oxygen and excited oxygen radicals. Due to the additional surface recombination at the chamber wall, more O_2 can be found near the wall. The number density of the ground state O_2 and its excited derivatives are demonstrated to be at the same order of magnitude as in shown (Tinck and Bogaerts, 2011) near the center plasma generation region.

The number densities of atomic oxygen-derived species (O, $O(^1D)$, and O^-) are shown in Fig. 6(d) and (e) and (f). The ground state atomic oxygen exists all the way to the outlet but its ionic and excited derivatives are contained at the reactor inlet. The high power adopted in this model enhances the ionization process as well as the conversion from O_2 to O and its radicals. However, because of the high activation energy of the atomic oxygen radicals, which are twice as big as the molecular oxygen radicals, they are more prone to return to ground states. Also, the ions are quickly de-ionized as soon as they enter the region with low electron density. This quick drop in the number densities of atomic oxygen ions and radicals has also been observed in (Tinck and Bogaerts, 2011).

It can be seen that the final product of the plasma generation domain is composed mostly of neutral atomic oxygen radicals, a small fraction of charged species, and a reasonable combination of ground state molecular oxygen and other excited species.

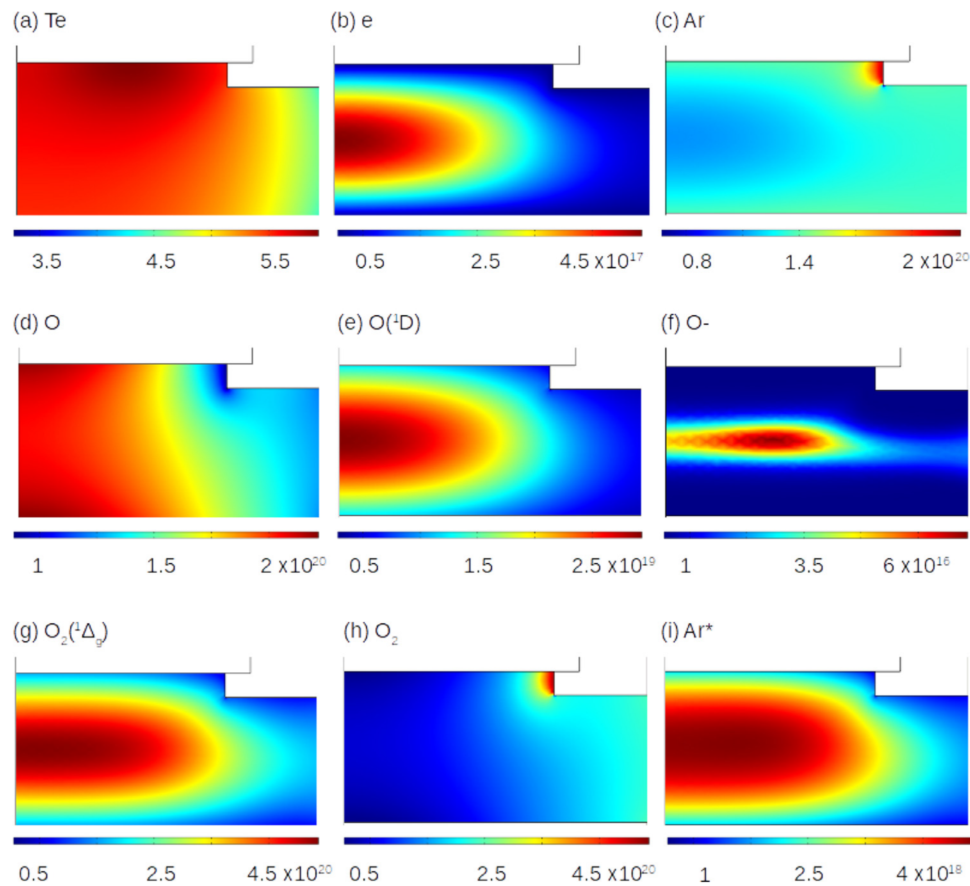

Fig. 6. Electron temperature and number densities of important plasma species. (For interpretation of the references to colour in this figure legend, the reader is referred to the web version of this article.)

The final molar fractions at the outlet region are: Ar, 2.80×10^{-1}; O_2, 5.39×10^{-1}; O, 1.65×10^{-1}; $O(^1D)$, 8.00×10^{-3}; Ar*, 2.74×10^{-3}; $O_2(^1\Delta_g)$, 2.67×10^{-3}; $O_2(^1\Sigma_g^+)$, 6.36×10^{-4}; O_2^+, 3.46×10^{-5}; O^+, 2.86×10^{-5} and O^-, 2.44×10^{-5}. After the plasma stream is introduced into the main reactor chamber, further recombination reactions will take place to reduce the plasma energy and minimize the impact of the charged species.

3.2. Main reactor gas transport

The gas-phase CFD model is tested over a wide range of precursor inputs, and it is demonstrated to successfully capture the macroscopic transport phenomena and reactions happening in the reactor chamber. The maximum Knudsen number in the reactor chamber under all operating conditions is around 0.05, which is much smaller than 0.1. Therefore, the continuum hypothesis is guaranteed at all parts of the reactor, and the Navier-Stokes equation can be safely used to solve for the fluid flow profile. Moreover, the maximum local Reynolds number is less than 200 and the fluid flow is entirely laminar. Therefore, turbulent modeling is not required in this simulation (Laurendeau, 2005).

First, we will investigate the reaction and transport in the main reactor chamber during the O-cycle, given a total of 450 sccm input from the plasma generation in COMSOL. The molar concentrations (number densities) of the important species in the reactor geometry are shown in Fig. 7, and the results are compared with respect to the established simulation models for plasma generation (Tinck and Bogaerts, 2011). As shown in Fig. 7(a), the oxygen gas molar concentration at the substrate surface and the outlet is about 1.1 to 2 times of the corresponding concentration at the inlet. This increase in the concentration is majorly contributed by two types of reactions: the de-excitation/de-ionization reactions of radicals and ions, and the gas-phase and surface recombination reactions of atomic oxygen. We can see from Fig. 7(c) that, for the radical species, $O_2(^1\Delta_g)$, its concentration remains fairly constant across the reactor despite its participation in the reactions that regenerate O_2, which mostly happened before crossing the showerhead. This is due to the fact that $O_2(^1\Delta_g)$ can be replenished from $O_2(^1\Sigma_g^+)$ in the downstream. On the other hand, the concentration of the other radical, $O_2(^1\Sigma_g^+)$, decreases rather fast and vanishes before the showerhead. Similarly, due to the high energy associated, the concentrations of positive and negative ions decrease in a similar trend to $O_2(^1\Sigma_g^+)$. Thus, nearly no ionic species is observed near the substrate.

As shown in Fig. 7(b), the atomic oxygen has a slight increase in concentration throughout the reactor. The rates of de-excitation and de-ionization of the atomic oxygen radicals and ions are extremely fast and cause those species to vanish right after entering the inlet. In particular, the singlet atomic oxygen species, according to the Tinck and Bogaerts (2011), recombine at a high rate in the main reactor gas transport, and will thus not be considered for the surface reaction. Meanwhile, a lot of ground state atomic oxygen is recombined into oxygen gas when it is in contact with the showerhead and the upstream reactor walls, which can be seen from the light regions and the sudden decrease of the concentration profile across the showerhead panel. However, it is demonstrated that not as much atomic oxygen is recombined to form oxygen gas as in Tinck and Bogaerts (2011). This is because the reactor pressure is higher, given the larger precursor flow and the compact showerhead reactor geometry, which leads to a smaller recombination co-

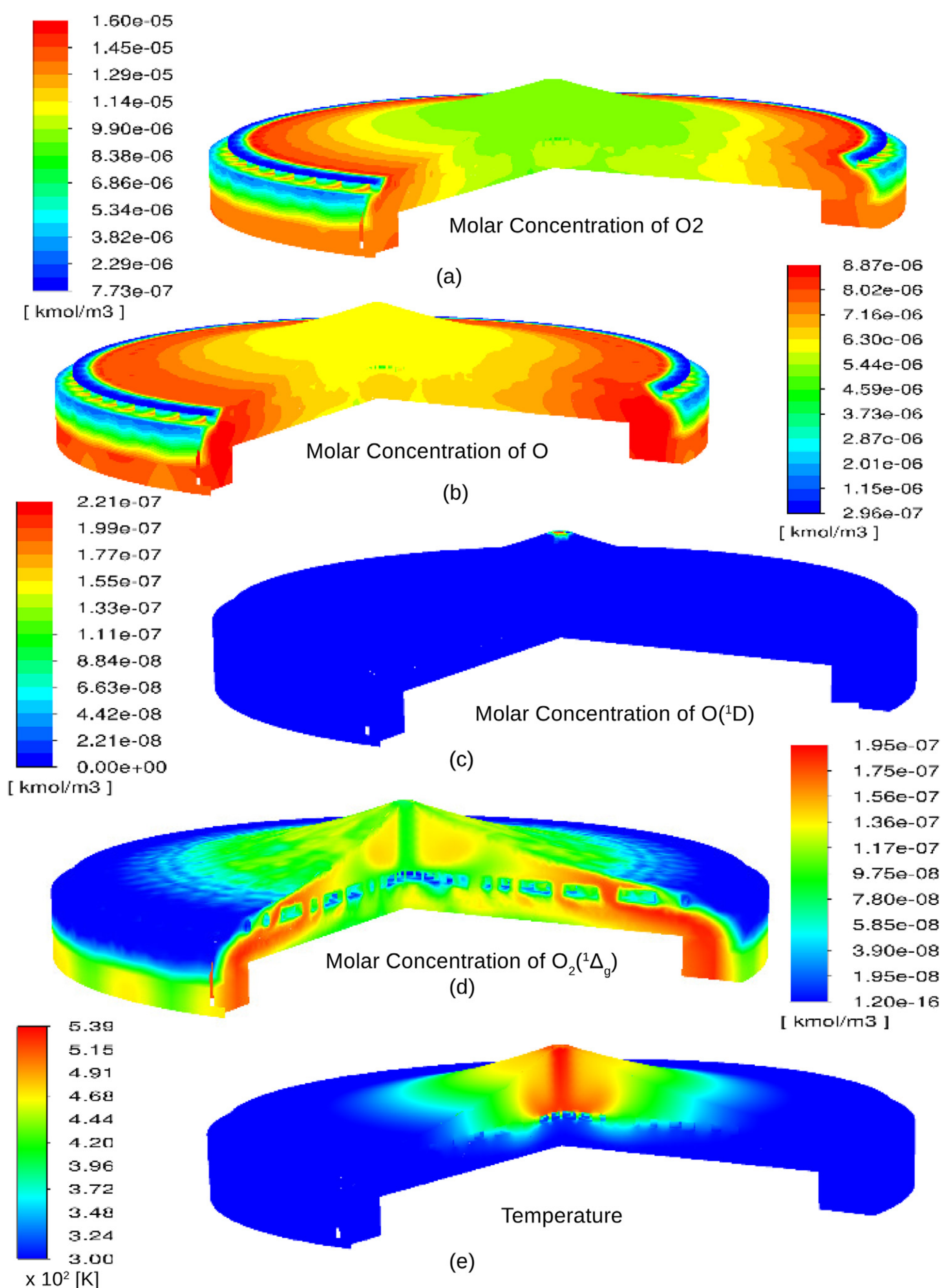

Fig. 7. Molar concentration of important species in the gas-phase CFD. (For interpretation of the references to colour in this figure legend, the reader is referred to the web version of this article.)

efficient. Still, the ratio of number density between the upstream and the top of the wafer are in reported ranges.

In addition, it can be seen in Fig. 7(e) that the region above the middle of the showerhead has a noticeably higher temperature than the rest of the reactor. This is caused by the huge extent of reaction in that region. In particular, charged particles like O^-, O^+, and O_2^+ are the major contributors to the heating due to their participation in the de-ionization reactions and the high-velocity kinetic impact, as demonstrated in (Joo and Rossnagel, 2009). As the gas species travel across the showerhead, the heat is less prone to transport to the downstream and is spread to the side of the reactor. Thus, the temperature on the substrate stays around 300 K, which is optimal for the temperature-sensitive materials and is much less likely for significant precursor decomposition to happen, which could lead to undesirable multiple-layer deposition reactions and surface island formation.

To further demonstrate the necessity of the showerhead design, we compare the gas-phase profile inside the reactor with and without a showerhead. For the reactor without a showerhead, the physics is axisymmetric and can be represented by a 2D axisymmetric model. The comparison of the velocity profile between the two models is shown in Fig. 8(a) and (b). Both velocity profile demonstrate that the middle of the reactor has a very high velocity under a high inlet flow rate of 450 sccm of argon and oxygen mixture. Without the showerhead, the velocity can still reach around 40 m/s at the substrate surface. In most applications, this high velocity is benign because the amoutn of ionic species that reach substrate is substantially reduced. However, it has been demon-

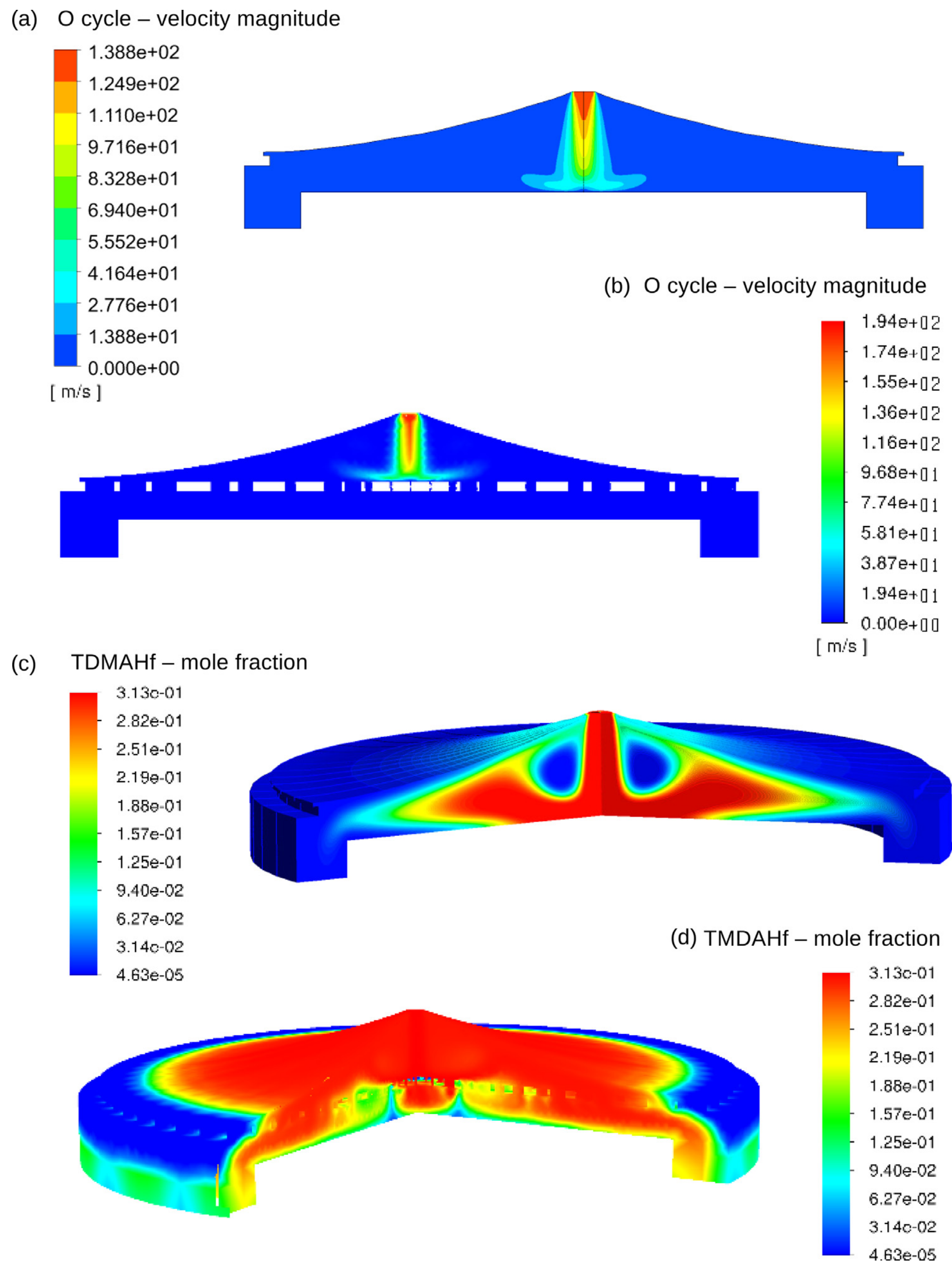

Fig. 8. Comparison of velocity profile and species transport between (a), (b) 2D and (c), (d) 3D models. (For interpretation of the references to colour in this figure legend, the reader is referred to the web version of this article.)

strated that in the PEALD of HfO_2 on graphene, defects due to ion species can still be observed even when remote oxygen plasma is used (Knoops et al., 2019). The observed high velocity in the center of the reactor may still lead to ion bombardment energy that is destructive to sensitive surfaces. Showerhead design is a solution to this problem. Even when the velocity at the inlet region is on the scale of a few hundred meters per second, the showerhead successfully blocks the fast traveling vertical gas flow in the center with the small showerhead holes, as shown in Fig. 8(b). Therefore, by having a showerhead panel, film damage through plasma distance and high inlet flow rate is minimized even for sensitive substrate surfaces. It is worth mentioning that the inclusion of the showerhead indeed slows down the vertical transport speed of the inlet species to the substrate surface, as shown in Fig. 8(c) and (d). Nevertheless, by optimizing the design of the showerhead panel, as shown in Fig. 3(d), the radial flow of the precursor is dramatically increased by assigning increasing diameter for the showerhead holes in the radial direction. Thus, with this enhanced guidance of gas flow towards the peripheral of the wafer, a much more uniform precursor distribution can be achieved on the substrate surface. Therefore, in order to capture the correct gas-phase profile, a full 3D model is helpful due to the showerhead design. However, the 2D axisymmetric model is less computationally demanding and can be used for an initial estimate for a wide range of operating conditions. In addition, experimental works, such as Joo and Rossnagel (2009), have demonstrated the strong dependency of thickness non-uniformity on the plasma pressure and chamber size. In our model, a similar maximum surface temperature around 500 K is observed under the corresponding plasma generation pressure, which validates the neutral heat transfer and the charged particle

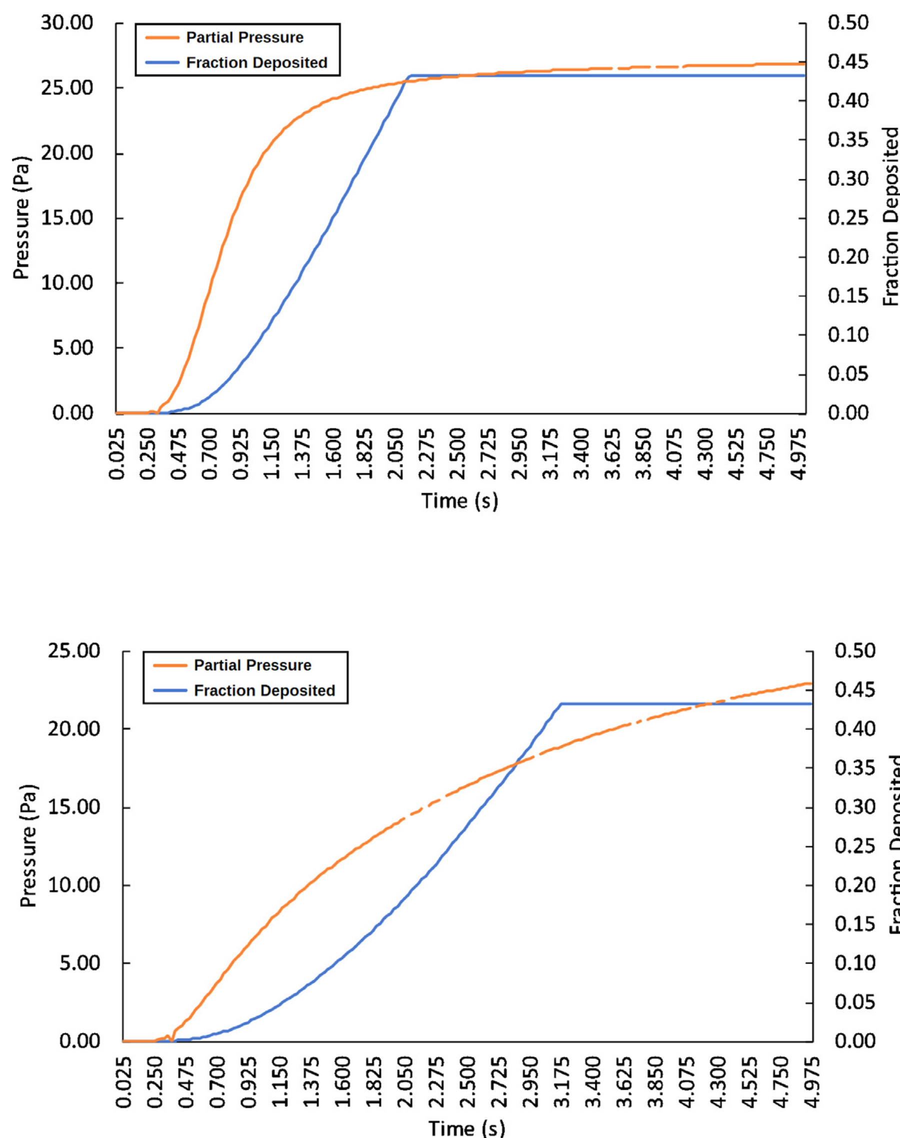

Fig. 9. Pressure development effect on Hf-cycle physisorption. (For interpretation of the references to colour in this figure legend, the reader is referred to the web version of this article.)

diffusion. However, we can see that the showerhead really endeavors to minimize the influence of the plasma operating parameters to the film uniformity. Thus, it allows more freedom for the plasma generator design without the need to worry about the negative effects on the subustrate uniformity and quality.

3.2.1. *Surface deposition*

The microscopic simulation of the surface deposition has been elaborated in Ding et al. (2020), where various operating parameters (operating temperature, precursor partial pressure, and etc.) are evaluated for their overall effects on the deposition rate by assuming a fixed surface profile for operating conditions. Under this assumption, a saturated GPC of around 1.17 Å per cycle is found to be achieved for the deposition of HfO_2 given sufficient precursor dosages at all time. Moreover, a range of different fixed operating conditions has been tested to obtain the critical precursor dosage that ensures both saturated GPC and low precursor waste. Despite the insights provided by the previous work on the overall trend, in a realistic deposition process, the precursor partial pressures and temperature are changing and are heavily influenced by the gas-phase species transport. Therefore, in this section, we look at the effect of time-dependent gas-phase profile on the microscopic surface deposition and the further validation of the deposition model based-on realistic gas-phase transport.

Studies were performed to derive the trend of pressure development using the 2D axisymmetric model, which is used to test the microscopic kMC model performance. Since the effect of steric hindrance is established in the Hf-Cycle, the preliminary studies focus on Hf-Cycle. The influence of partial pressure development on the fraction of sites that are physisorbed is demonstrated in Fig. 9. Specifically, under a high inlet flow rate of 300 sccm of TDMAHf and Ar, the precursor partial pressure saturates around 2.5 s, and the surface physisorption can finish at 2.275 s. By contrast, under a low inlet flow rate of 150 sccm TDMAHf and Ar, the precursor partial pressure does not achieve full saturation until the end of Hf-cycle, and the surface physisorption takes around 3 s. In addition, the temperature influence on the deposition rate is similar to what has been learned in Ding et al. (2020). Moreover, our studies demonstrate that given sufficient precursor dosages, the surfaces are guaranteed to reach saturation coverage (limited by the steric hindrance). Under those operating conditions, a linear growth profile can be ob-

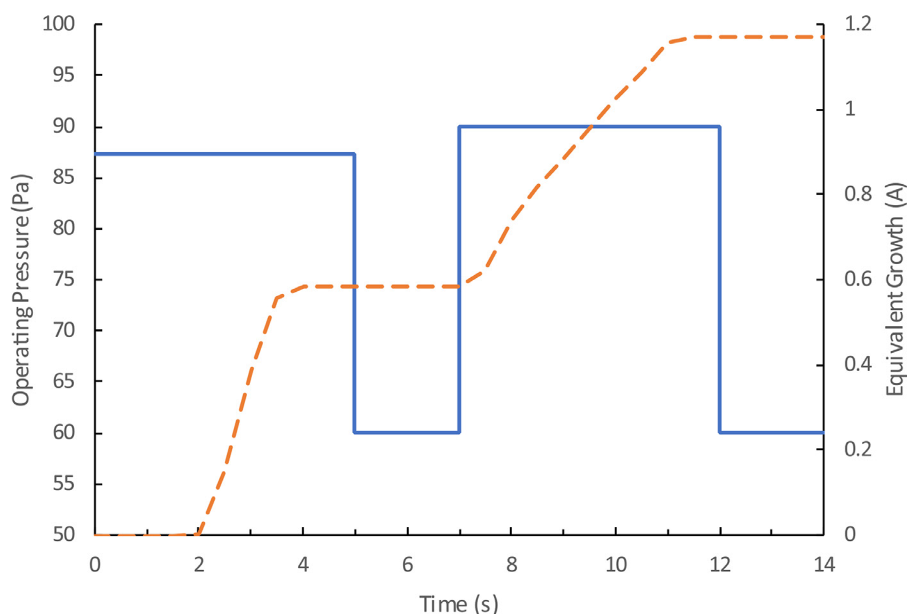

Fig. 10. Operating baseline and average deposition rate. *x*-axis is time, left *y*-axis is the operating pressure and right *y*-axis is the effective average growth over the entire substrate surface. The orange dashed line represents the change in the effective average thickness and the solid blue line represent the change in operating pressure. (For interpretation of the references to colour in this figure legend, the reader is referred to the web version of this article.)

Table 5
Summary of the assumptions and results of each domain in the multiscale CFD model.

	Assumptions
Plasma Domain	Decoupled completely from other domains
Main-Chamber Domain	Incompressible ideal gas in continuum regime
Surface Domain	Depends only on surface pressure, temperature and configuration
	Results
Plasma Domain	Steady-states are achieved in a short timescale (~ 10^{-3} s)
Main-Chamber Domain	Realistic profiles are obtained under typical feed flow rates (~ 150 sccm)
Surface Domain	An overall growth per cycle (GPC) of 1.17 Å/Cycle is observed

served for multi-cycle deposition as reported in the experimental works.

3.2.2. Integrated ALD chamber design and evaluation

After each simulation scale is validated, all model components are integrated for the final multiscale analysis as indicated in Section 2.5. Based on literature references and preliminary calculations from individual models, an operating baseline is tested as shown in Fig. 10, which consists of a 5 s TDMAHf pulse at 87.25 Pa, followed by a 5 s oxygen plasma pulse at a pressure of 90 Pa, while each precursor pulse is separated by 2 s of purging and pumping down to a base pressure of 60 Pa. The base operating pressure is achieved with a constant 300 sccm flow of argon carrier gas, and the effective precursor molar flow rate for Hf-Cycle and O-Cycle is 137 sccm and 150 sccm, respectively. Unlike the experimental GPC measurement using ellipsometry and X-ray photoelectron spectroscopy (XPS), the simulation model does not directly report the height of the deposited thin-film because of the lattice approximation adopted. However, GPC can be calculated using the coverage and lattice information. A GPC of 1.17 Å/Cycle can be achieved given enough precursor dosage, which is similar to the experimental results with comparable operating conditions (Choi et al., 2004; Lao et al., 2005; Park et al., 2006). Also, the simulation model shows a linear growth for multi-cycle deposition, as observed in the experimental works by Liu et al. (2005) and Provine et al. (2016). A summary of the assumptions and the general results of the developed multiscale CFD model is included in Table 5.

In addition to the overall growth, it is important to investigate the spatial difference in the deposition profile. Non-uniformity is often encountered in large wafer production, but the lack of low-cost and straightforward in-situ monitoring techniques makes it difficult to find out the problem during the manufaturing process. With the multiscale CFD model, we can analyze the gas-phase flow profile and the surface deposition profile to reduce non-uniformity through reactor geometry optimization and operating parameter adjustment. The major non-uniformity often occurs along the radial direction. Therefore, the analysis on the entire substrate is divided into three zones according to their respective radius: central region (0 to 50 mm), middle region (50 to 100 mm), and peripheral region (100 to 150 mm). The deposition development profiles at those three regions are shown in Fig. 11. With the aid of the showerhead and the horn-shaped upstream, the flow of the precursors is guided in the radial direction, the transient film non-uniformity is substantially reduced, and the final influence of this non-uniformity is eliminated within the prescribed cycle time for both cycles.

Utilizing the multiscale simulation model, we have investigated a potential way of reducing the required cycle time by effectively utilizing initial period of the purge step for deposition. Purge step has always been solely used to clear out the remaining precursor, assuming that surface deposition is finished within each precursor half-cycle time. This is because the amount of precursors remaining on the wafer during purging cannot be accurately measured and the resulted contribution to the deposition is not well understood. Nevertheless, the developed multiscale CFD model is

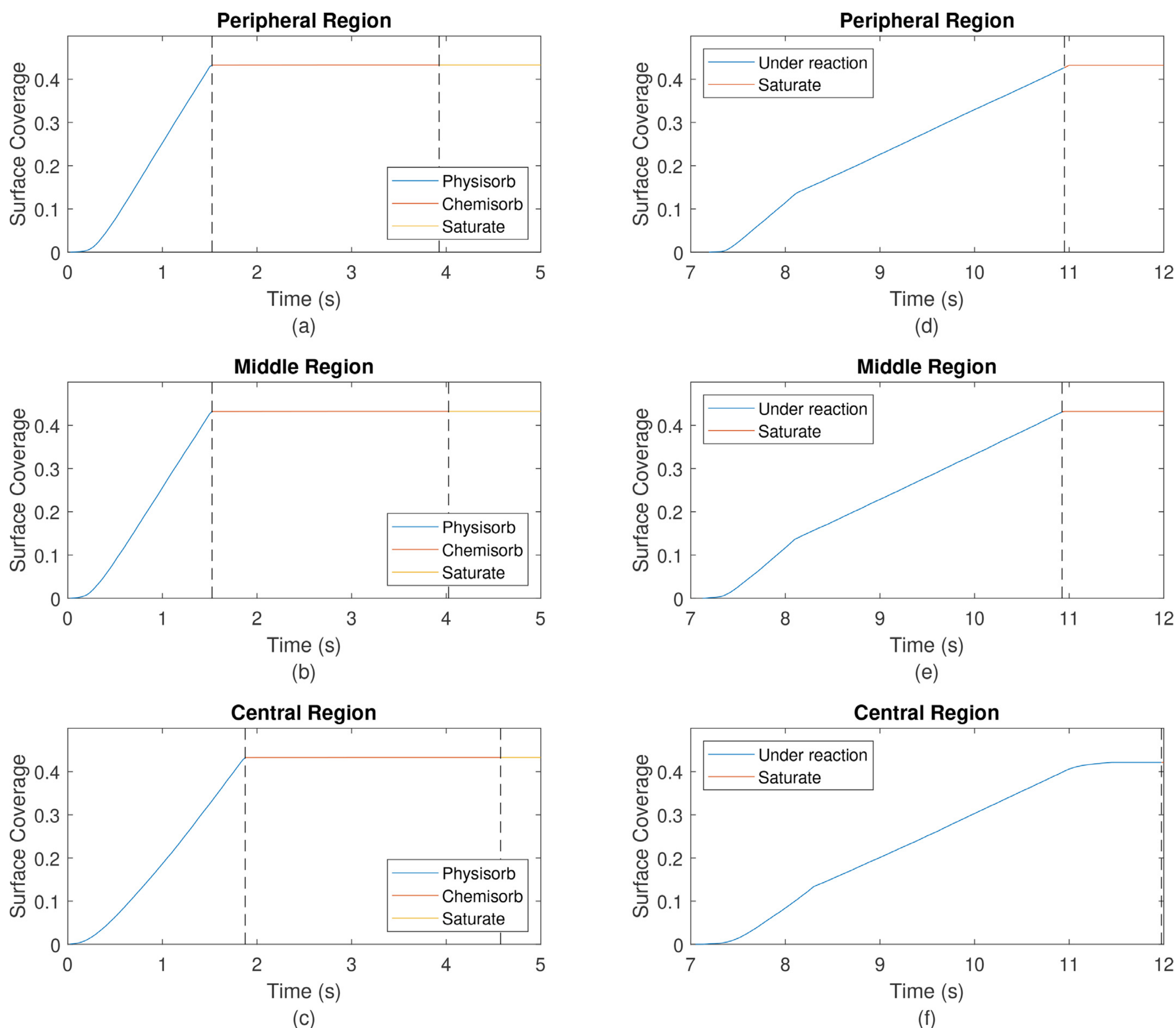

Fig. 11. (a), (b), (c) Hf-Cycle deposition profiles of the peripheral, middle, and central regions of the substrate, respectively. The blue line represents the time duration for TDMAHf physisorption, the red line represents the time duration for TDMAHf chemisorption and the orange line represents the time duration after the surface is saturated. (d), (e), (f) O-Cycle deposition profiles of the peripheral, middle, and central regions of the substrate. The blue line represents the time duration for O-Cycle deposition reaction and the red line represents the time duration after the surface is saturated. (For interpretation of the references to colour in this figure legend, the reader is referred to the web version of this article.)

able to capture the exact amount of precursor existing on the surface and the associated rate of surface reactions. From simulation results, we observe that the surface partial pressure of both precursors could retain at a decent level during the initial time steps. The middle region, which is demonstrated to have the slowest deposition rate, has even longer residual time. Therefore, these remaining precursor will still lead to a high enough physisorption rate, thus maintaining the equilibrium for the subsequent forward chemisorptions. A case study on O-Cycle is performed using the baseline operating temperature and pressure, with a reduced O-Cycle time of 4 s. The overall surface deposition at the end of O-Cycle is found to be 97.4% of the saturation coverage, and the center has a lower value of 87%. After we shift to the purging, the overall wafer is found to retain 50% of the remaining precursors at 0.2 s, and the center is found to retain 42% of the remaining precursors at 0.4 s, which will continue to contribute to the surface physisorption. At the end of the purge step, all precursors are cleared out and the entire surface reaches full coverage. Thereby, the O-cycle time can be reduced by 20%, and a even higher reduction can be achieved in Hf-cycle. As a result, it is demonstrated that the remaining precursor is able to provide a significant contribution to the deposition during both Hf-cycle and O-cycle purging.

4. Conclusion

In this work, we have constructed a multiscale CFD model for the plasma-enhanced atomic layer deposition of HfO_2 using TDMAHf and oxygen plasma. The remote plasma generation model and the macroscopic gas-phase CFD model are constructed and coupled with the previously developed microscopic kMC model through an automated workflow. Both macroscopic domains were individually validated against experimental and existing single

scale simulation data. Specifically, the detailed plasma profile was analyzed in both the plasma domain and the gas-phase domain, in which the species transport and plasma reactions across the reactor chamber were correctly captured. The multiscale model was validated and utilized to identify the effects of plasma generation power, operating pressure, operating temperature, and inlet flow rates on the deposition of HfO_2 thin-films. The model output was demonstrated to be consistent with the overall trend reported from literature and industrial specifications. Furthermore, using the multiscale CFD model, a set of baseline operating parameters were determined to produce highly uniform HfO_2 thin-film within conventional industrial half-cycle time, and the transient non-uniformity across the entire substrate was successfully reduced under the baseline operating conditions. In addition, the model was adopted to investigate the possibility of reducing the total operation time by at least 14.3% from efficiently taking advantage of the remaining precursors at the beginning of the purge steps. This work provides a general-purpose tool to explore the optimal operating conditions under which a thin-film can be produced with guaranteed quality with a significantly reduced process operation time. Using this model, process optimization strategies can be determined, thereby greatly increasing production throughput.

Declaration of Competing Interest

The authors declare that they have no known competing financial interests or personal relationships that could have appeared to influence the work reported in this paper.

CRediT authorship contribution statement

Yichi Zhang: Conceptualization, Methodology, Software. **Yangyao Ding:** Conceptualization, Methodology, Software. **Panagiotis D. Christofides:** Supervision, Writing - review & editing.

Acknowledgments

Financial support from the National Science Foundation is gratefully acknowledged.

References

Bird, R.B., Stewart, W.E., Lightfoot, E.N., 2007. Transport Phenomena. John Wiley & Sons.
Chaffart, D., Ricardez-Sandoval, L.A., 2017. Robust dynamic optimization in heterogeneous multiscale catalytic flow reactors using polynomial chaos expansion. J. Process Control 60, 128–140.
Chaffart, D., Ricardez-Sandoval, L.A., 2018. Optimization and control of a thin film growth process: a hybrid first principles/artificial neural network based multiscale modelling approach. Comput. Chem. Eng. 119, 465–479.
Check, C.E., Faust, T.O., Bailey, J.M., Wright, B.J., Gilbert, T.M., Sunderlin, L.S., 2001. Addition of polarization and diffuse functions to the LANL2DZ basis set for p-block elements. J. Phys. Chem. A 105, 8111–8116.
Choi, S., Koo, J., Jeon, H., Kim, Y., 2004. Plasma-enhanced atomic-layer deposition of a HfO_2 gate dielectric. J. Korean Phys. Soc. 44, 35–38.
Corr, C., Gomez, S., Graham, W., 2012. Discharge kinetics of inductively coupled oxygen plasmas: experiment and model. Plasma Sources Sci. Technol. 21, 055024.
Cortright, R.D., Dumesic, J.A., 2001. Kinetics of heterogeneous catalytic reactions: analysis of reaction schemes. Adv. Catal. 46, 161–264.
Courant, R., Friedrichs, K., Lewy, H., 1967. On the partial difference equations of mathematical physics. IBM J. Res. Dev. 11 (2), 215–234.
Crose, M., Zhang, W., Tran, A., Christofides, P.D., 2018. Multiscale three-dimensional CFD modeling for PECVD of amorphous silicon thin films. Comput. Chem. Eng. 113, 184–195.
Ding, Y., Zhang, Y., Kim, K., Tran, A., Wu, Z., Christofides, P.D., 2019. Microscopic modeling and optimal operation of thermal atomic layer deposition. Chem. Eng. Res. Des. 145, 159–172.
Ding, Y., Zhang, Y., Orkoulas, G., Christofides, P.D., 2020. Microscopic modeling and optimal operation of plasma enhanced atomic layer deposition. Chem. Eng. Res. Des. 159, 439–454.
Dkhissi, A., Estève, A., Mastail, C., Olivier, S., Mazaleyrat, G., Jeloaica, L., Djafari-Rouhani, M., 2008. Multiscale modeling of the atomic layer deposition of Hfo_2 thin film grown on silicon: how to deal with a kinetic monte carlo procedure. J. Chem. Theory Comput. 4, 1915–1927.
Dorsmann, R., Kleijn, C.R., 2007. A general correction to surface reaction models based on reactive sticking coefficients. Chem. Vap. Deposit. 13, 91–97.
Elliott, S.D., Greer, J.C., 2004. Simulating the atomic layer deposition of alumina from first principles. J. Mater. Chem. 14, 3246–3250.
Epelle, E.I., Gerogiorgis, D.I., 2017. A multiparametric CFD analysis of multiphase annular flows for oil and gas drilling applications. Comput. Chem. Eng. 106, 645–661.
Eymard, R., Gallouët, T., Herbin, R., 2000. Finite volume methods. Handbook Numer. Anal. 7, 713–1018.
Fluent, A., 2013. Ansys fluent theory guide 15.0. ANSYS, Canonsburg, PA.
Frisch, A., Nielsen, A.B., Holder, A.J., 2000. Gaussview user manual. Gaussian Inc., Pittsburgh, PA 556.
Garcia, A.L., Alder, B.J., 1998. Generation of the chapman–enskog distribution. J. Comput. Phys. 140, 66–70.
George, S.M., 2009. Atomic layer deposition: an overview. Chem. Rev. 110, 111–131.
Gerogiorgis, D.I., Ydstie, B., 2005. Multiphysics CFD modelling for design and simulation of a multiphase chemical reactor. Chem. Eng. Res. Des. 83, 603–610.
Hausmann, D.M., Kim, E., Becker, J., Gordon, R.G., 2002. Atomic layer deposition of hafnium and zirconium oxides using metal amide precursors. Chem. Mater. 14, 4350–4358.
Hay, P.J., Wadt, W.R., 1985. Ab initio effective core potentials for molecular calculations. Potentials for K to Au including the outermost core orbitals. J. Chem. Phys. 82 (1), 299–310.
Hay, P.J., Wadt, W.R., 1985. Ab initio effective core potentials for molecular calculations. Potentials for the transition metal atoms Sc to Hg. J. Chem. Phys. 82 (1), 270–283.
Heil, S., Van Hemmen, J., Hodson, C., Singh, N., Klootwijk, J., Roozeboom, F., Van de Sanden, M., Kessels, W., 2007. Deposition of TiN and HfO_2 in a commercial 200 mm remote plasma atomic layer deposition reactor. J. Vacuum Sci. Technol. A 25, 1357–1366.
Huang, J., Hu, G., Orkoulas, G., Christofides, P.D., 2010. Dependence of film surface roughness and slope on surface migration and lattice size in thin film deposition processes. Chem. Eng. Sci. 65, 6101–6111.
Ishikawa, K., Karahashi, K., Ichiki, T., Chang, J.P., George, S.M., Kessels, W., Lee, H.J., Tinck, S., Um, J.H., Kinoshita, K., 2017. Progress and prospects in nanoscale dry processes: how can we control atomic layer reactions? Jpn. J. Appl. Phys. 56, 06HA02.
Jeon, H., Won, Y., 2008. The reaction pathways of the oxygen plasma pulse in the hafnium oxide atomic layer deposition process. Appl. Phys. Lett. 93 (12), 124104.
Jeon, H.-T., Kim, I.-H., Kim, S.-H., Chung, C.-W., Lee, S.-K., 2007. Apparatus for generating remote plasma. US Patent App. 11/703, 621.
Jeong, S.-J., Gu, Y., Heo, J., Yang, J., Lee, C.-S., Lee, M.-H., Lee, Y., Kim, H., Park, S., Hwang, S., 2016. Thickness scaling of atomic-layer-deposited HfO_2 films and their application to wafer-scale graphene tunnelling transistors. Sci. Rep. 6, 20907.
Joo, J., Rossnagel, S.M., 2009. Plasma modeling of a PEALD system for the deposition of TiO_2 and HfO_2. J. Korean Phys. Soc. 54, 1048.
Kanomata, K., Pansila, P., Ahmmad, B., Kubota, S., Hirahara, K., Hirose, F., 2014. Infrared study on room-temperature atomic layer deposition of TiO_2 using tetrakis (dimethylamino) titanium and remote-plasma-excited water vapor. Appl. Surf. Sci. 308, 328–332.
King, S.W., 2011. Plasma enhanced atomic layer deposition of SiN_x:H and SiO_2. J. Vacuum Sci. Technol. A 29, 041501.
Knoops, H.C., Faraz, T., Arts, K., Kessels, W.M., 2019. Status and prospects of plasma-assisted atomic layer deposition. J. Vacuum Sci. Technol. A 37, 030902.
Kukli, K., Ritala, M., Schuisky, M., Leskelä, M., Sajavaara, T., Keinonen, J., Uustare, T., Hårsta, A., 2000. Atomic layer deposition of titanium oxide from TiI_4 and H_2O_2. Chem. Vap. Deposit. 6, 303–310.
Kumar, N., George, B.P.A., Abrahamse, H., Parashar, V., Ray, S.S., Ngila, J.C., 2017. A novel approach to low-temperature synthesis of cubic Hfo_2 nanostructures and their cytotoxicity. Sci. Rep. 7, 1–14.
Kwon, J.S.-I., Nayhouse, M., Orkoulas, G., Ni, D., Christofides, P.D., 2015. A method for handling batch-to-batch parametric drift using moving horizon estimation: application to run-to-run MPC of batch crystallization. Chem. Eng. Sci. 127, 210–219.
Kwon, J.S.-I., Nayhouse, M., Orkoulas, G., Ni, D., Christofides, P.D., 2015. Run-to-run-based model predictive control of protein crystal shape in batch crystallization. Ind. Eng. Chem. Res. 54, 4293–4302.
Lao, S.X., Martin, R.M., Chang, J.P., 2005. Plasma enhanced atomic layer deposition of HfO_2 and ZrO_2 high-k thin films. J. Vacuum Sci. Technol. A 23, 488–496.
Laurendeau, N.M., 2005. Statistical thermodynamics: Fundamentals and applications. Cambridge University Press.
Lee, C., Graves, D., Lieberman, M., Hess, D., 1994. Global model of plasma chemistry in a high density oxygen discharge. J. Electrochem. Soc. 141, 1546–1555.
Lee, C., Lieberman, M., 1995. Global model of Ar, O_2, Cl_2, and Ar/O_2 high-density plasma discharges. J. Vacuum Sci. Technol. A 13, 368–380.
Lee, C. S., Oh, M. S., Park, H. S., 2006. Plasma enhanced atomic layer deposition (PEALD) equipment and method of forming a conducting thin film using the same thereof. US Patent 7, 138, 336.
Liu, X., Ramanathan, S., Longdergan, A., Srivastava, A., Lee, E., Seidel, T.E., Barton, J.T., Pang, D., Gordon, R.G., 2005. ALD Of hafnium oxide thin films from tetrakis (ethylmethylamino) hafnium and ozone. J. Electrochem. Soc. 152, G213–G219.

Liu, X., Ramanathan, S., Seidel, T.E., 2003. Atomic layer deposition of hafnium oxide thin films from tetrakis (dimethylamino) hafnium (TDMAH) and ozone. MRS Online Proc. Library Arch. 765.

Liu, Y., Liu, H., 2018. Development of 3D polymer DFT and its application to molecular transport through a surfactant-covered interface. AlChE J. 64, 238–249.

Moura, C.A.d., Kubrusly, C.S., 2012. The Courant-Friedrichs-Lewy (CFL) Condition: 80 Years After Its Discovery. Birkhäuser Basel.

Multiphysics, C., 1998. Introduction to COMSOL multiphysics®. COMSOL Multiphysics, Burlington, MA, accessed Feb 9, 2018.

Nalwa, H. (Ed.), 2002. Handbook of Thin Films. Vol. 1. Academic Press, Burlington.

Oh, S.-K., Lee, J.M., 2016. Iterative learning model predictive control for constrained multivariable control of batch processes. Comput. Chem. Eng. 93, 284–292.

Pan, D., Li, T., Chien Jen, T., Yuan, C., 2014. Numerical modeling of carrier gas flow in atomic layer deposition vacuum reactor: a comparative study of lattice boltzmann models. J. Vacuum Sci. Technol. A 32, 01A110.

Park, P.K., Roh, J.-S., Choi, B.H., Kang, S.-W., 2006. Interfacial layer properties of HfO_2 films formed by plasma-enhanced atomic layer deposition on silicon. Electrochem. Solid-State Lett. 9, F34–F37.

Pittal, S., Snyder, P.G., Ianno, N.J., 1993. Ellipsometry study of non-uniform lateral growth of ZnO thin films. Thin Solid Films 233, 286–288.

Profijt, H., Potts, S., Van de Sanden, M., Kessels, W., 2011. Plasma-assisted atomic layer deposition: basics, opportunities, and challenges. J. Vacuum Sci. Technol. A 29, 050801.

Provine, J., Schindler, P., Torgersen, J., Kim, H.J., Karnthaler, H.-P., Prinz, F.B., 2016. Atomic layer deposition by reaction of molecular oxygen with tetrakisdimethylamido-metal precursors. J. Vacuum Sci. Technol. A 34, 01A138.

Rai, V.R., Vandalon, V., Agarwal, S., 2010. Surface reaction mechanisms during ozone and oxygen plasma assisted atomic layer deposition of aluminum oxide. Langmuir 26, 13732–13735.

Rasoulian, S., Ricardez-Sandoval, L.A., 2015. Robust multivariable estimation and control in an epitaxial thin film growth process under uncertainty. J. Process. Control 34, 70–81.

Rasoulian, S., Ricardez-Sandoval, L.A., 2016. Stochastic nonlinear model predictive control applied to a thin film deposition process under uncertainty. Chem. Eng. Sci. 140, 90–103.

Rey, J.C., Cheng, L., McVittie, J.P., Saraswat, K.C., 1991. Monte Carlo low pressure deposition profile simulations. J. Vacuum Sci. Technol. A 9, 1083–1087.

Ribes, G., Mitard, J., Denais, M., Bruyere, S., Monsieur, F., Parthasarathy, C., Vincent, E., Ghibaudo, G., 2005. Review on high-k dielectrics reliability issues. IEEE Trans. Device Mater. Reliab. 5, 5–19.

Schuegraf, K., Abraham, M.C., Brand, A., Naik, M., Thakur, R., 2013. Semiconductor logic technology innovation to achieve sub-10 nm manufacturing. IEEE J. Electron Devices Soc. 1, 66–75.

Schwille, M.C., Schössler, T., Barth, J., Knaut, M., Schön, F., Höchst, A., Oettel, M., Bartha, J., 2017. Experimental and simulation approach for process optimization of atomic layer deposited thin films in high aspect ratio 3D structures. J. Vacuum Sci. Technol. A 35, 01B118.

Shi, X., Tielens, H., Takeoka, S., Nakabayashi, T., Nyns, L., Adelmann, C., Delabie, A., Schram, T., Ragnarsson, L., Schaekers, M., et al., 2011. Development of ALD $HfZrO_x$ with TDEAH/TDEAZ and H_2O. J. Electrochem. Soc. 158, H69–H74.

Shirazi, M., Elliott, S.D., 2014. Atomistic kinetic monte carlo study of atomic layer deposition derived from density functional theory. J. Comput. Chem. 35, 244–259.

Tinck, S., Bogaerts, A., 2011. Computer simulations of an oxygen inductively coupled plasma used for plasma-assisted atomic layer deposition. Plasma Sources Sci. Technol. 20, 015008.

Wadt, W.R., Hay, P.J., 1985. Ab initio effective core potentials for molecular calculations. Potentials for main group elements Na to Bi. J. Chem. Phys. 82 (1), 284–298.

Wang, Y., Gao, F., Doyle, F.J., 2009. Survey on iterative learning control, repetitive control, and run-to-run control. J. Process Control 19, 1589–1600.

Won, T. K., Nominanda, H., Cho, S.-M., Choi, S. Y., Park, B. S., White, J. M., Anwar, S., Kudela, J., 2014. Thin film deposition using microwave plasma. US Patent 8, 883, 269.

Won, Y., Park, S., Koo, J., Kim, S., Kim, J., Jeon, H., 2005. Initial reaction of hafnium oxide deposited by remote plasma atomic layer deposition method. Appl. Phys. Lett. 87, 262901.

Yun, S.J., Lim, J.W., Lee, J.-H., 2004. PEALD of zirconium oxide using tetrakis (ethylmethylamino) zirconium and oxygen. Electrochem. Solid-State Lett. 7, F81–F84.

Zhang, Y., Ding, Y., Christofides, P.D., 2019. Multiscale computational fluid dynamics modeling of thermal atomic layer deposition with application to chamber design. Chem. Eng. Res. Des. 147, 529–544.

Zhang, Y., Ding, Y., Christofides, P.D., 2020. Integrating feedback control and run-to-run control in multi-wafer thermal atomic layer deposition of thin films. Processes 8, 18.